DEPOSITED DIELECTRICS WITH LOW CRYOGENIC MICROWAVE LOSS AND THEIR ROOM TEMPERATURE PROPERTIES

BRUNO BUIJTENDORP

Master Thesis
Submitted for the degree of:

Master of Science (MSc) in Applied Physics

Thesis committee:

dr. A. Endo,
TU Delft, Faculty of EEMCS, Department of Microelectronics,
TU Delft, Faculty of Applied Sciences, Department of Quantum Nanoscience
dr. S. Vollebregt,
TU Delft, Faculty of EEMCS, Department of Microelectronics
prof. dr. G. Steele,
TU Delft, Faculty of Applied Sciences, Department of Quantum Nanoscience

Degree obtained at:

Delft University of Technology
Faculty of Applied Sciences
Department of Quantum Nanoscience

November 2019

ABSTRACT

Superconducting resonators used in mm/sub-mm (MMW) astronomy would greatly benefit from deposited dielectrics with low dielectric loss. The excess loss in deposited dielectrics is mainly due to two-level systems (TLS), and there is no consensus on their microscopic origin.

To study the relation between hydrogenated amorphous silicon's (a-Si:H) microwave (MW) loss at 120 mK and its void volume fraction, hydrogen content, microstructure parameter, bond-angle disorder, and infrared (IR) refractive index, we deposited films at substrate temperatures of 100°C, 250°C and 350°C using plasma-enhanced chemical vapor deposition (PECVD).

We measured the room temperature properties of the films using Fourier-transform infrared spectroscopy, Raman spectroscopy and ellipsometry. All room temperature properties except the IR refractive index decrease monotonically with increasing substrate temperature. The IR refractive index approaches the refractive index of crystalline silicon (c-Si) when increasing the substrate temperature to 350 °C.

We measured the dielectric losses using superconducting coplanar waveguide resonators. Interestingly, we do not see a correlation of the room temperature results with the MW losses. All films have an excellent 120 mK MW loss tangent below 10^{-5} at -50 dBm internal resonator power. More research on the loss tangents is recommended, for example using microstrip lines or lumped element parallel plate capacitors.

The low dielectric losses make these films promising for application in MW kinetic inductance detectors and on-chip filters. These promising results could lead to the application of the dielectrics in the integrated superconducting spectrometer DESHIMA 2.0.

ACKNOWLEDGMENTS

I want to express my gratitude to my thesis supervisors, Akira Endo and Sten Vollebregt, who have always been very enthusiastic in helping me with this project. I appreciate a lot how they have encouraged me to be guided by my own curiosity. They were always willing to go the extra mile in their support for my project and both of them display a passion for their work that is contagious. I am very enthusiastic about the prospect of having them as my PhD supervisors in the coming years.

I am thankful to Gary Steele for devoting his time to being a committee member for this thesis, and also for responding enthusiastically and bringing me in contact with his research group when I reached out to him with questions at an early stage of this project.

I want to thank Jochem Baselmans, who has been very helpful in the many discussions that we have had about this project. I always learned a lot during these discussions, and his passion for his research has inspired me. I am thankful to Juan Bueno who has been very generous with his time while helping me with the measurements at SRON, and has always been eager to answer all my questions.

David Thoen also deserves my gratitude, I am grateful for how much he has helped me with the cleanroom work, and for his eagerness to teach me. I also express my gratitude to Marco van der Krogt, who has helped me with many depositions.

I want to thank Paolo Sberna, who has been my cleanroom mentor during the start of this project, and who has also deposited the first films for me. I very much appreciate his help during that time. I am also grateful to Vignesh Murugesan, who has patterned all the chips that were used for this project. I want to thank Sebastian Hähnle, Pieter de Visser, and Kevin Kouwenhoven who have enthusiastically provided their input for this project.

Last but not least I thank everybody from the THz Sensing group, because I am sure that there are many people that deserve my gratitude that I have not mentioned, but also for the fun that I have had during my time as a master student in this group.

CONTENTS

LIST OF FIGURES

LIST OF TABLES

1 INTRODUCTION

By looking at distant galaxies, we are looking at a distant past. The light from these early galaxies has travelled for more than a billion years before reaching Earth. These galaxies were covered in dust, which makes them difficult to detect from their visible and ultraviolet radiation [55]. To unravel the secrets of the star formation and galaxy evolution in the early universe, we need instruments that can detect the mm/sub-mm (MMW) radiation that was re-emitted by the dust that surrounded these galaxies.

Due to the large distance between these galaxies and Earth, their radiation is faint and we need very sensitive detectors. Furthermore, because the radiation from these far-away galaxies is redshifted due to the expansion of the universe, we need wide-band spectrometers to study the wide range of redshifts that cover the time span of these evolutionary processes.

The answer to these problems is the integrated superconducting spectrometer (ISS) [8, 10, 44]. It is a superconducting circuit on a chip of a few cm^2, that contains a filterbank for dispersion of the incoming radiation, and microwave kinetic inductance detectors (MKIDs) for photon detection. It delivers the wide-band, high-sensitivity spectroscopy that is required to study the early universe. With the first light demonstration of the DESHIMA project on the Atacama Submillimeter Telescope Experiment (ASTE), the ISS technology has recently performed its first astronomical observation [11].

1.1 MOTIVATION

In comparison with the coplanar waveguide (CPW) transmision lines that are currently used in DESHIMA, microstrips have the advantage that they can be made smaller, allowing more circuit elements to fit on a chip. Additionally, microstrip filters do not suffer from the excitation of a common mode that causes large radiation losses [17, 21].

A disadvantage of microstrips is that they cannot easily be fabricated with a crystalline dielectric. Deposited dielectrics suffer from excess dielectric loss at cryogenic temperatures. Although this loss is successfully modelled by two-level systems (TLS) [38, 54], there is no consensus on its microscopic origin [34].

Our work on low-loss deposited dielectrics is motivated by its application in the lossless MMW microstrip-based circuit elements, including filters, for the next generation of DESHIMA. An improved dielectric would also be beneficial for applications in other fields, for

example in superconducting qubits [36], nano-mechanical resonators [39], and gravitational wave detectors [31]. Additionally, an improved understanding is interesting from a fundamental perspective.

1.2 HYPOTHESIS AND RESEARCH METHOD

The status quo in the MKID community is that hydrogenated amorphous silicon (a-Si:H) is the most promising low-loss deposited dielectric [29]. We have identified recent literature that is disputing the superiority of a-Si:H over amorphous silicon (a-Si) [26, 41].

According to these authors, hydrogen and the passivation of dangling bonds are not necessary to diminish the TLS. Instead, a correlation with the density of the dielectric was found, and the proposed cause of the TLS is voids in the material. A drastic reduction of the TLS density and voids was realized by depositing at elevated substrate temperatures (T_{sub}).

This leads us to the hypothesis that the dielectric loss in a-Si:H stems from voids in the material, and that it can be reduced by depositing at high substrate temperatures.

To test this hypothesis, we measured the 120 mK microwave (MW) dielectric loss of three a-Si:H films, deposited at different substrate temperatures with plasma-enhanced chemical vapor deposition (PECVD).

We designed a chip that uses superconducting resonators to measure the dielectric losses. In addition to these measurements, we characterized the films at room temperature to learn more about their structure and composition.

From ellipsometry measurements we derived the films' void volume fractions. Using Fourier-transform infrared (FTIR) spectroscopy, we measured the hydrogen content and the microstructure parameter, which are both related to voids in the dielectric [3, 45]. From the same measurement we obtained the infrared (IR) refractive index. Using Raman spectroscopy we measured the bond-angle disorder, giving us information about the disorder in the a-Si network that is hosting the voids.

Additionally, we deposited an amorphous silicon carbide (a-SiC) film using PECVD, and measured its dielectric loss and IR refractive index. Earlier films that were deposited using this recipe were known to have no voids, making it an interesting case for testing our hypothesis on a material other than a-Si:H.

1.3 THESIS OUTLINE

Chapter 2 two gives a more in-depth discussion on the literature that has guided our hypothesis, and we show the historical path that has

led to the status quo on the superiority of PECVD a-Si:H. Additionally, we summarize what is currently known about the microstructure and composition of a-Si:H, and how this relates to this research.

In chapter 3 we introduce the plasma-enhanced chemical vapor deposition (PECVD) process. We show the parameters that affect the film deposition, and the recipes that we used to deposit our films. Finally, we show the results of the stress measurements and discuss blistering in one of the films.

Chapters 4, 5 and 6 are about the room temperature characterizations: the Fourier-transform infrared (FTIR) spectroscopy, Raman and ellipsometry. We introduce the basics of these methods, we explain the data analysis, and we give the results.

Chapter 7 concerns the design of the chip that was used to measure the microwave loss tangents. We explain how it functions a a loss measurement device, our design considerations, its coupler and frequency design and its sensitivity to the dielectric loss.

In chapter 8 we discuss the dielectric loss measurements. After a description of the measurement principle, we discuss the calculation of the filling fractions of the films. Then we show the measured internal quality factors of the resonators, and we calculate upper limits of the loss tangents. We end this chapter with an estimate of the loss tangents using a reference measurement on c-Si.

Finally, in chapter 9 we give a conclusion, followed by recommendations for future work.

2 LITERATURE STUDY

2.1 A NEW INSIGHT IN LOW-LOSS DEPOSITED DIELECTRICS

Our hypothesis was guided by the discovery of a paper that disputes the superiority of a-Si:H over a-Si [26]. Interestingly, the first author of this paper is also the author of the 1997 and 1998 papers [24, 25] that have led to this consensus in the MKID community [29].

Before the new research by Liu and Queen et al. it was assumed that hydrogen played an essential role in minimizing the loss in a-Si:H [24, 39]. Liu et al. deposited hydrogen-free films using e-beam evaporation in a T_{sub} range from (45 - 400 °C). The films with a T_{sub} of 350 °C or higher had a TLS density as low as the best hydrogenated films.

They measured the dangling bond density using electron spin resonance (ESR) spectroscopy, and concluded that dangling bonds and their passivation by hydrogen have no effect on the TLS density. Based on a correlation with film density, but not with the films' elastic properties, their conclusion is that the TLS in a-Si and in a-Si:H come from voids inside the dielectric [41]. They propose that the microscopic tunneling entities that form the TLS could be groups of atoms on the surface of voids [40].

The choice for a-Si:H by Mazin et al. in 2010 was based on a 2008 paper from the superconducting qubit community by O'Connel et al. [36]. In this paper the authors compared the dielectric losses of various deposited dielectrics, and concluded that a-Si:H has the lowest loss. They were guided by earlier research by Pohl, Liu and Thompson from 2002 [39].

In this paper an overview of the TLS density obtained from internal friction measurements was given for a broad range of dielectrics. The most promising candidate was a-Si:H that was deposited by hot wire chemical vapor deposition (HWCVD), followed by PECVD a-Si:H.

Now, Liu and Queen reinterpret these older results [26]. In the original comparison of a-Si:H with a-Si films, the a-Si:H films were deposited at elevated T_{sub} and the e-beam films at near room temperature. This was what differentiated the a-Si:H from the a-Si films, not the hydrogen and its passivation of dangling bonds.

2.2 A DISORDERED NETWORK WITH VOIDS

Since our hypothesis is about the occurrence of voids in the dielectric, we aim to find correlations of the dielectrics microscopic structure

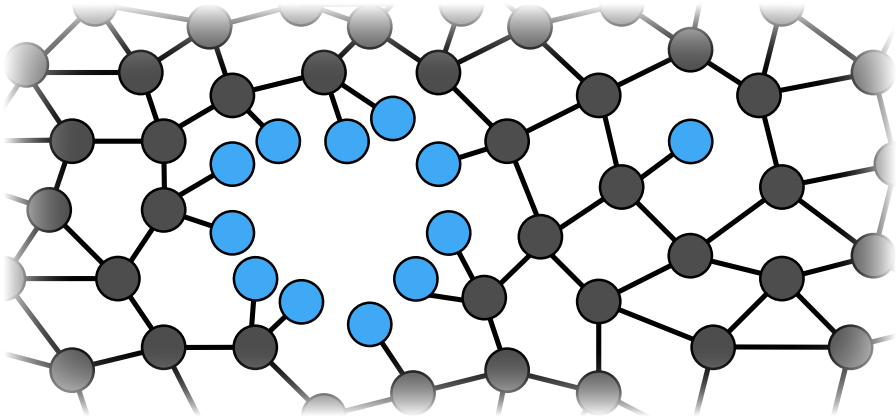

Figure 1: Illustration of a void and a monovacancy in a-Si:H. The grey circles represent Si atoms, the blue circles represent hydrogen atoms.

with its dielectric loss. In this section we give an overview of what we know about the microstructure of a-Si:H, including voids, and its relation to the hydrogen bonding configurations in the material.

Amorphous silicon is fourfold coordinated: The Si atoms are bound to four other atoms. The Si atoms are bound in a tetrahedral structure, but there is no long-range order. Because the hydrogen atoms in a-Si:H only bind to one atom, they act as terminators of the a-Si:H network. Due to this termination by hydrogen, there are only three possible tetrahedrons that can contribute to the network: Si_4H, Si_3H_2 and Si_2H_3, which we simply denote as SiH, SiH_2 and SiH_3.

Given the ratio of hydrogen to silicon in the a-Si:H, the probabilities for these three configurations to occur can be calculated [33]. From this it follow that for an atomic fraction of H below 40%, the number of atoms that are bound in SiH_3 configurations is negligible [33]. This means that when we study the microstructure using Fourier-transform infrared (FTIR) spectroscopy, we can focus on the effects of SiH and SiH_2.

It is known that the microstructure of a-Si:H is largely governed by the occurrence of SiH and SiH_2 in the material [37]. A study using nuclear magnetic resonance (NMR) has shown that the SiH and SiH_2 do not only reside in isolated vacancies, but also in groups [37]. It has been found that at hydrogen concentrations above 14 at.%, voids are formed in the a-Si:H network. We have measured the hydrogen content of our a-Si:H films using FTIR.

In contrast to the SiH configurations that also exist in monovacancies, the SiH_2 configurations exist mainly on the surfaces of voids with a radius of 1 - 4 nm [45]. Therefore, by studying the concentration of SiH and SiH_2 bonds with FTIR, we gain additional insight into the microstructure of the a-Si:H, that complements our ellipsometry measurement of the void volume fraction.

Deposition at elevated substrate temperatures does not only lead to a decrease in the amount of voids, due to enhanced surface energetics

[26], but it also makes the a-Si:H network more rigid. To acquire information on the rigidity of the network, and also the amorphicity of the dielectric, we measure the network's bond angle disorder using Raman spectroscopy.

3

DEPOSITION OF THE DIELECTRICS

The a-Si:H and a-SiC films were deposited using plasma-enhanced chemical vapor deposition (PECVD). In the first section of this chapter we introduce the concept of PECVD, we list the parameters that can influence the process, and we explain the recipes that we have used.

In the second section we discuss the quality of the resulting films: we are interested in films with low stress and without blisters. Low-stress films are required for the application of our dielectrics in the relatively thick (one micron) dielectric layers in the microstrips of the next generation of the DESHIMA spectroscopic chip that was discussed in Chapter 1. Films without blisters are desired because blisters are a form of delamination of the film, and therefore can result in broken circuit elements. Their occurrence makes the deposition process unreliable.

3.1 PLASMA-ENHANCED CHEMICAL VAPOR DEPOSITION

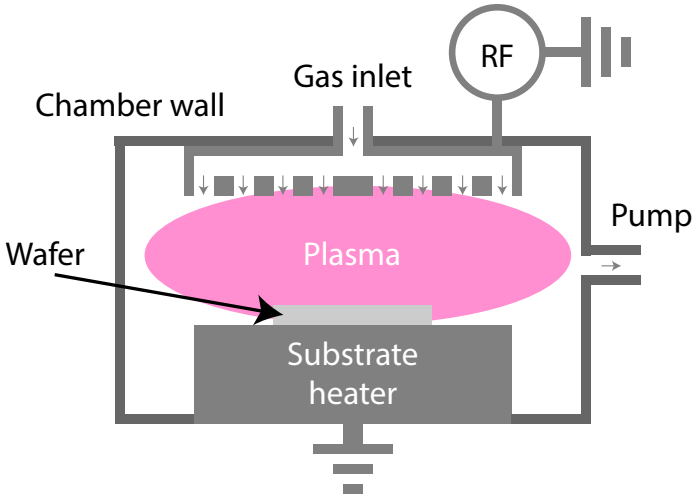

Figure 2: Schematic of a PECVD machine. The temperature of the substrate heater is the deposition parameter of our focus.

The name of this process is derived from the plasma that is sustained between the two electrodes, and that energizes the gas and makes it reactive. Inside the plasma, a chemical reaction occurs, and the film is grown by the adsorption of the reactant gasses with the substrate.

The plasma is ignited by a radio frequency (RF) source, which is connected to the top electrode. Optionally, an additional low fre-

quency (LF) source can be used, as we do in our a-SiC deposition. Before the reactant gases flow into the plasma chamber, the chamber is pumped to near vacuum (below 1 mTorr) to prevent ambient contaminations.

The machine that we used for the a-SiC deposition has a load lock. In this case, the wafer is placed in a wafer holder inside the load lock, and after the load lock has been pumped to vacuum, the wafer is automatically transferred to the process chamber. In this way the process chamber can maintain its vacuum, thereby reducing the processing time and further protecting the process chamber from ambient contaminations.

As we can see in Fig. 2, the top electrode of the PECVD machine functions as a so-called shower head for the gas inlet, where the precursor and dilution gasses flow in. In the deposition of a-Si:H the precursor gas is silane (SiH_4), and in our process we use the noble gas argon (Ar) as a dilution gas. In the a-SiC deposition, there are two precursor gasses: SiH_4 and methane (CH_4), but no dilution gasses. The gasses in the process chamber are pumped away to maintain a constant pressure.

During the deposition, the wafer is resting on a substrate heater, which typically has a temperature between 250 and 400 °C. The substrate temperature (T_{sub}) is the parameter of our focus, because we are testing the hypothesis that the dielectric loss in a-Si:H stems from voids in the material, and that it can be reduced by depositing at high T_{sub}.

The machine that was used for the a-Si:H films was an Oxford Instruments Plasmalab 80 Plus. For the a-SiC we used a Novellus Concept 1.

3.1.1 *Process parameters*

The deposition parameters that influence the process are:

- Substrate temperature (T_{sub})
- RF power
- LF power
- Gas flow rates
- Chamber pressure
- Deposition time

In addition to these user-defined parameters, the process is also influenced by the chamber volume and the electrode spacing. Because the effects of the deposition parameters are interrelated, it is not trivial to predict the effect of an individual deposition parameter [13]. For the

same reason it is hard to compare the effects of individual process parameters with literature.

3.1.2 *Recipes*

In our depositions of a-Si:H we vary only T_{sub}. The 250 °C recipe is our starting point. This recipe has been supplied by Oxford Instruments, the manufacturer of the PECVD machine. This recipe was designed to produce amorphous films with almost zero stress. The SiC recipe was developed in our faculty at DIMES, now called the Else Kooi Lab, and is also known to produce films with very low stress [43]. In Table 1 the recipes for the four different materials are given.

The target thickness of all the films was 250 nm. Estimations on the required deposition times to obtain this thickness were made by linearly interpolating the records of past deposition times and thicknesses.

Material	a-Si:H 100 / 250 / 350	a-SiC
T_{sub} (°C)	100 / 250 / 350	400
RF power (W)	15	450
LF power (W)	-	150
SiH_4 flow (sccm)	25	25
Ar flow (sccm)	475	0
CH_4 flow (sccm)	-	411
Pressure (Torr)	1	2
Dep. time (m's")	10'0" / 7'9" / 7"	0'26"

Table 1: PECVD recipes.

3.2 RESIDUAL STRESS AND BLISTERS

3.2.1 *Stress measurement principle*

The wafer stress is measured by a system that moves a laser beam over the wafer along an axis parallel to the wafer surface. A position sensitive photo diode is used to measure the deflection of the laser beam by the wafer. In doing so, the machine is able to calculate the radius of curvature of the wafer along this axis. This has to be done before and after the deposition of the film. Then, using the Stoney equation, the stress in the deposited thin film can be calculated [1]:

$$\sigma = \frac{E_s}{6(1-\nu_s)} \frac{t_s^2}{t_f} \left(\frac{1}{R} - \frac{1}{R_0} \right). \tag{1}$$

Here the subscripts s and f denote the substrate and the film, E is the Young's modulus, ν is Poisson's ratio, t denotes thickness, R_0 is the radius of curvature before deposition and R is the radius of curvature after deposition.

3.2.2 *Stress measurement results*

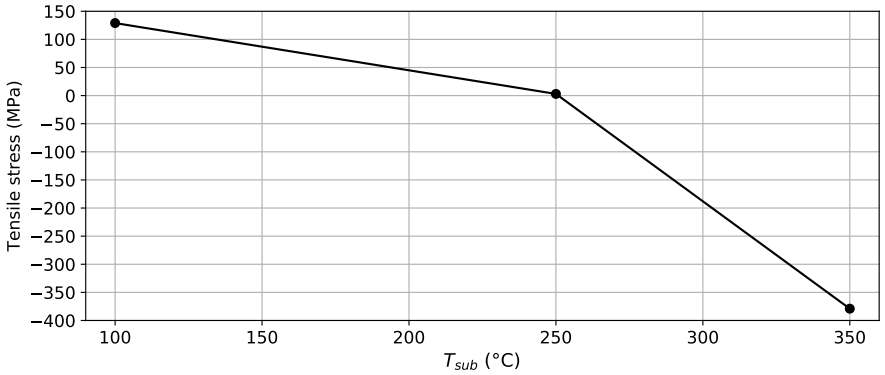

Figure 3: Measured stresses of the a-Si:H films. Positive stress denotes tensile stress.

Both the 250 °C and the a-SiC recipes were known beforehand to produce films with almost zero residual stress. In Fig. 3 we see a plot of the stresses of the a-Si:H films, and in Table 2 we have listed all measured stresses. We see that the a-Si:H film deposited at 250 °C indeed has almost zero stress. The stress in the a-Si:H becomes tensile when depositing at lower temperatures, and it becomes compressive when depositing at higher temperatures. As expected, the a-SiC film has a very low compressive stress, of only 20 MPa.

	a-Si 100	a-Si 250	a-Si 350	a-SiC
σ (MPa)	129	3	-379	-20

Table 2: Measured thin-film residual stress, a positive number denotes tensile stress.

3.2.3 *Occurrence of blisters*

Blisters are circular sections of the film where the film is buckled and therefore not attached to the substrate anymore, but the film is still intact.

The 100 °C a-Si, the 250 °C a-Si and the a-SiC films did not have blisters in all three depositions using the same recipe. All three 350 °C films have circular blisters of approximately 0.1 mm in diameter. It might be that the blistering in the 350 °C film is occurring due

to the compressive stress of this film, since buckling is a commonly occurring phenomenon for films under compressive stress.

4 FOURIER TRANSFORM INFRARED SPECTROSCOPY

In Section 2.2 we have explained the relation between the hydrogen bonding configurations in a-Si:H and the microstructure of the dielectric. By measuring the concentrations of these bonding configurations, we gain insight into the microstructure of the material. Fourier transform infrared spectroscopy (FTIR) allows us to measure these concentrations. In this chapter we explain the principle of FTIR, and how we applied it to learn more about the microstructure of a-Si:H.

Additionally, from the FTIR measurement we get the infrared refractive index (n_{ir}). This is not only an indication of the density of the films, but it is also used to estimate the MMW refractive index, as is explained in Appendix C. For the microstructure analysis we have limited ourselves to a-Si:H, but we also measured the n_{ir} of the a-SiC film.

4.1 MEASUREMENT PRINCIPLE

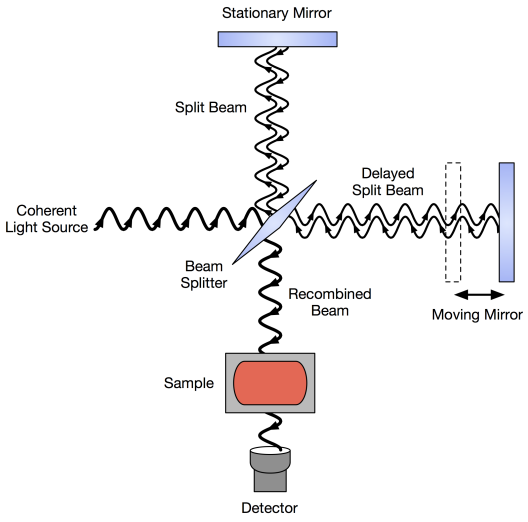

Figure 4: Illustration of how an FTIR spectrometer works.

An FTIR spectrometer measures the transmission through a wafer, and does this simultaneously in a wide wavenumber range (400 - 4000 cm^{-1}, or equivalently, 120 to 12 THz), and with high spectral resolution. Because the chemical bonds inside the dielectric absorb photons at distinct frequencies, by measuring the transmission spectrum with FTIR we can see what kinds of chemical bonds there are, and we can see their concentrations.

Instead of shining a single frequency at the sample, measuring the transmission, and repeating this for every frequency, the FTIR spectrometer does something more clever. The infrared (IR) source shines its entire frequency band at a Michelson-interferometer simultaneously. One of the mirrors of the interferometer is moved, thereby periodically blocking each frequency. The raw data is the transmission as a function of mirror position. A Fourier transform is used to convert this data into the transmission as a function of wavenumber. This is where the instrument's name comes from. An illustration of this mechnaism is shown in Fig. 4.

Our measurements were done with a Thermo Fischer Nicolet FTIR spectrometer, with a wave-number resolution of 4 cm^{-1}.

4.2 FROM TRANSMISSION DATA TO ABSORPTION COEFFICIENTS

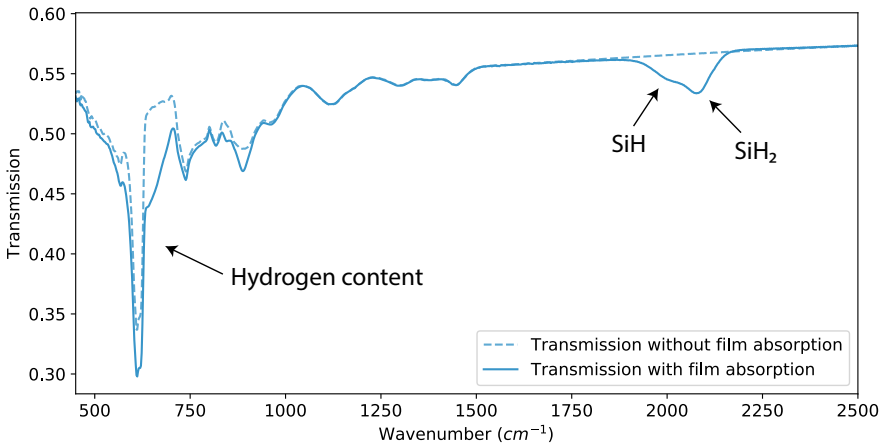

Figure 5: The absorptions of interest in a-Si:H. The transmission with film absorption is measured on the 100 °C film. The transmission without film absorption is calculated, this is explained in Section 4.5. The difference between the dashed and solid line shows the absorption of the deposited film.

From the FTIR measurements we get the transmission through the wafer as a function of wavenumber ($T(\nu)$). In Fig. 5 we can see the transmission through a wafer with an a-Si:H film that was deposited at 100 °C. In addition to the wagging mode around 640 cm^{-1} that is used to calculate the hydrogen content, and the stretching modes around 2000, and 2100 cm^{-1} that are used to calculate the microstructure parameter (R^*), we can also clearly see an absorption around 890 cm^{-1} which is due to the bending mode of SiH_2 [7].

To calculate the parameters that tell us something about the film's microstructure, we first have to convert $T(\nu)$ to the absorption coefficients ($\alpha(\nu)$). Due to the multiple internal reflections in the film, we cannot simply use the Lambert-Beer law for this.

Instead, we use the transfer-matrix method (TMM), which is a method to calculate the transmission and reflection coefficients of a multi-layer optical system. It can be derived directly from the Maxwell equations, more specifically from the continuity conditions for the electric field across a boundary [6]. In Section 4.5 we discuss our application of this method.

Another often used method to determine $\alpha(\nu)$ from $T(\nu)$ is commonly referred to as the BCC method [5]:

$$T = \frac{4T_0^2 e^{-\alpha d}}{(1+T_0)^2 - (1-T_0)^2 e^{-2\alpha d}}. \tag{2}$$

This optical model assumes incoherent transmission in both the film and the substrate, and it assumes that there are no reflections at the film-substrate interface. An improvement to this method that takes the reflections at this interface and interference inside the thin-film into account is given by Maley [27] and by Tzolov et al. [50]. Swanepoel has investigated the effect of inhomogeneities in film thickness and refractive index on the transmission spectrum [49].

4.3 OBTAINING THE MICROSTRUCTURE PARAMETER

In Section 2.2 we have seen that the concentrations of the SiH and SiH_2 bonding configurations are related to the microstructure of the a-Si:H films: The SiH_2 configurations reside mainly on the inner surface of voids. The microstructure parameter (R^*) tells us what fraction of the hydrogen is bonded as SiH_2, and therefore it is related to the void density [37].

Before we can calculate this parameter, we first have to calculate the integrated absorptions of the SiH and SiH_2 bonding configurations. The integrated absorption of a bonding configuration centered around wavenumber x is:

$$I_x = \int_x \frac{\alpha(\nu)}{\nu} d\nu. \tag{3}$$

As we can see in Fig. 5, the absorptions of the stretching modes of SiH and SiH_2 are centered around 2000 cm^{-1} and 2100 cm^{-1}. From their integrated absorptions we can calculate R^*:

$$R^* = \frac{I_{2100}}{I_{2100} + I_{2000}}. \tag{4}$$

4.4 CALCULATING THE HYDROGEN CONTENT

The hydrogen content is another parameter that we want to measure because it is related to the microstructure of our a-Si:H films. It is defined as:

$$C_H = \frac{N_H}{N_H + N_{Si}} \text{ at.\%}. \tag{5}$$

Here N_H and N_{Si} are the number densities (atoms per unit volume) of hydrogen and c-Si. Note that N_{Si} is the number density of c-Si, not of the amorphous silicon layer. Therefore this fraction does not represent the true atomic percentage of hydrogen in the film. The hydrogen content is also often defined as the fraction N_H/N_{Si}. The number density of c-Si is:

$$N_{Si} = 5 \cdot 10^{22} \text{ cm}^{-3}, \tag{6}$$

and N_H is calculated as:

$$N_H = A_{640} \cdot I_{640}, \tag{7}$$

where I_{640} is the integrated absorption of the wagging mode at 640 cm^{-1}, and A_{640} is a proportionality constant that is a cross-section for photon absorption at this frequency. All three hydrogen bonding configurations (SiH, SiH_2, SiH_3) contribute to I_{640}, and therefore it is a measure of the total hydrogen content [37, 48]. The proportionality constant can be determined by measuring the hydrogen content by other means. We use the following constant [22]:

$$A_{640} = 2.1 \cdot 10^{19} \text{ cm}^{-2}. \tag{8}$$

4.5 APPLICATION OF THE TRANSFER-MATRIX METHOD

As was explained in Section 4.2, we use the TMM method to obtain the $\alpha(\nu)$ of the film. In the process we also get n_{ir}. In the fitting of the measured $T(\nu)$ to the TMM calculation, n and k are the free parameters that we obtain from this fit. For the film thickness, which is a parameter in the model, we use the values that were measured using ellipsometry. These values are listed in Table 5. For the implementation of the TMM we used the Python module *tmm* [6].

4.5.1 *Modeling the substrate*

Because the c-Si substrate has significant absorptions in the measurement range of 400 to 4000 cm^{-1}, that must be included in the TMM model, we first measure the substrate absorption by performing an FTIR measurement on the bare substrate. The substrate extinction coefficient $k(\nu)$ is retrieved from the measurement by fitting it to the TMM calculation.

The substrate $k(\nu)$ is fitted separately for each wavenumber, such that the simulated substrate transmission is exactly equal to the measured substrate transmission. Fitting a continuous function $k(\nu)$ for the substrate absorption is not necessary since we are not interested in characterizing the substrate absorption, and also it would not result in a good fit because of the complex and sharp absorption profile of the substrate.

Because of the large thickness of the substrate (about 0.5 mm), the interference fringes due to reflection inside the substrate are too narrow to be sampled by the FTIR measurement, even at the highest possible resolution of our instrument, which is 1 cm^{-1}. In combination with a curved baseline - meaning non-horizontal transmission in case of no absorption - this makes it unpractical to obtain the substrate n from the FTIR measurement itself. Additionally, the refractive index of c-Si in this wavenumber range has been measured by many authors and is nearly constant in this range. For these reasons we use the standard literature value of 3.42 for the n of the substrate [22]. Additional details of the substrate transmission and modeling, including figures, can be found in Appendix B.

Obtaining the thin-film complex refractive index

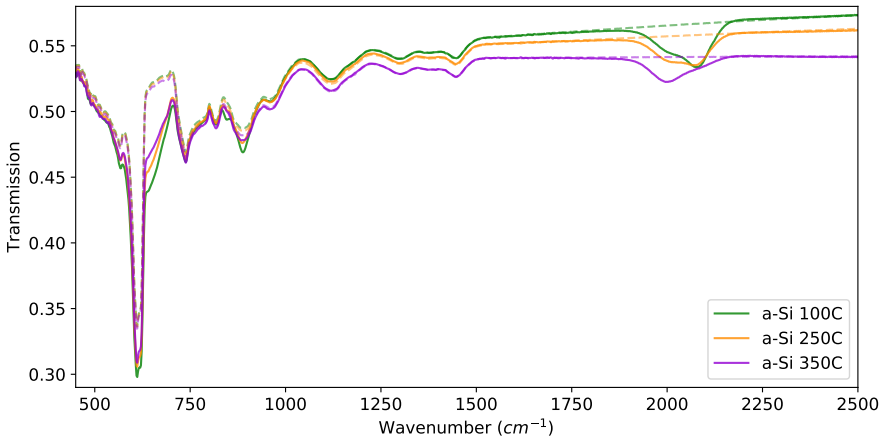

Figure 6: The solid lines are the measured transmissions of the a-Si:H films, the dashed line is the TMM calculation using the fitted n, without film absorptions.

The refractive index (n) is obtained by fitting the TMM model with zero film absorption to the measurement. The resulting TMM calculations for a-Si:H can be seen in Fig. 6. The same calculation is also performed to obtain the n of a-SiC.

The absorption regions are excluded from the fitting of n. We use the obtained n in a second TMM calculation, from which we get $k(\nu)$. Then a sum of Gaussians is fitted to the resulting $k(\nu)$ to get the absorption spectra of the bond types of interest. The results are discussed in the next section.

4.6 RESULTS

From our FTIR measurements we have obtained n_{ir} for the a-Si:H and a-SiC films, and for the a-Si:H films we have also obtained R^* and C_{H}.

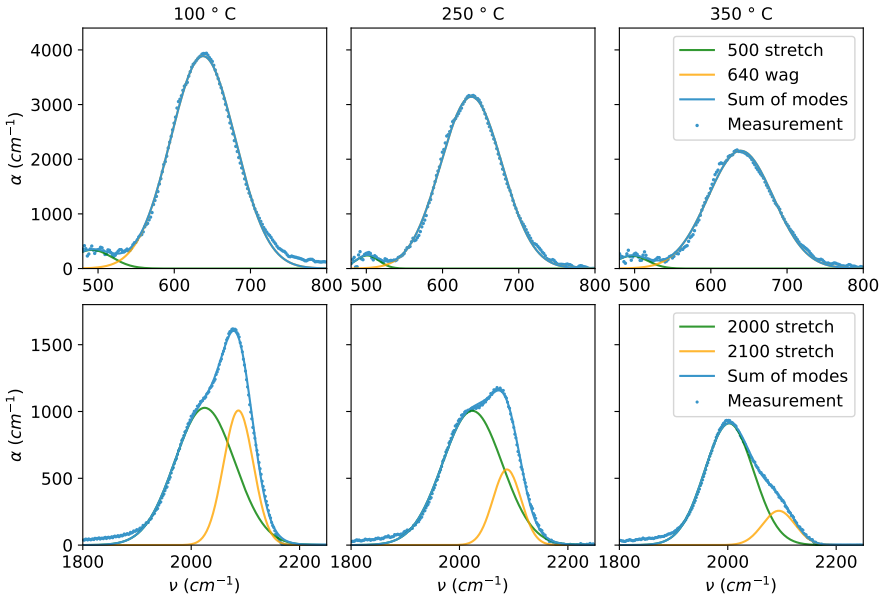

Figure 7: Absorption coefficient spectra of the the a-Si:H films. The top row shows the absorption that is used to calculate C_H. The bottom row shows the absorptions that are used to calculate R^*.

In Fig. 6 the differences in n between the three a-Si:H films can clearly be seen from the inclinations of the absorption-less transmissions. We can see that the absorption-less transmission of the 350 °C film is nearly horizontal because the n approaches the n of the substrate.

In Fig. 7 we can see the a-Si:H absorption coefficient spectra $\alpha(\nu)$ that were calculated with the TMM. The top row shows the peaks from which C_H can be calculated. The bottom row shows the peaks from which we calculate R^*. A clear temperature dependence of the total hydrogen content and the SiH_2 stretching mode can immediately be seen.

Fig. 8 and Table 3 show all the calculated parameters. For the three a-Si:H films we see a monotonic decrease of both C_H and R^* with T_{sub}. The infrared refractive index increases monotonically with T_{sub} and approaches 99% of the refractive index of c-Si for the highest substrate temperature of 350 °C.

Finally, we note that in the absorption coefficient plots (Fig. 7), a bump is visible around 500 cm^{-1}. This comes from a Si-Si stretching mode and was included in the fit [27]. The bottom row shows a misalignment of the fit at the edges. This could be due to the fact that this calculation is not Kramers-Kronig (KK) consistent. In reality n and k are related through the KK-relations, and therefore the use of a constant n is not correct in the vicinity of these absorptions. An iterative procedure can be used to calculate a KK-consistent complex refractive index using our method [18].

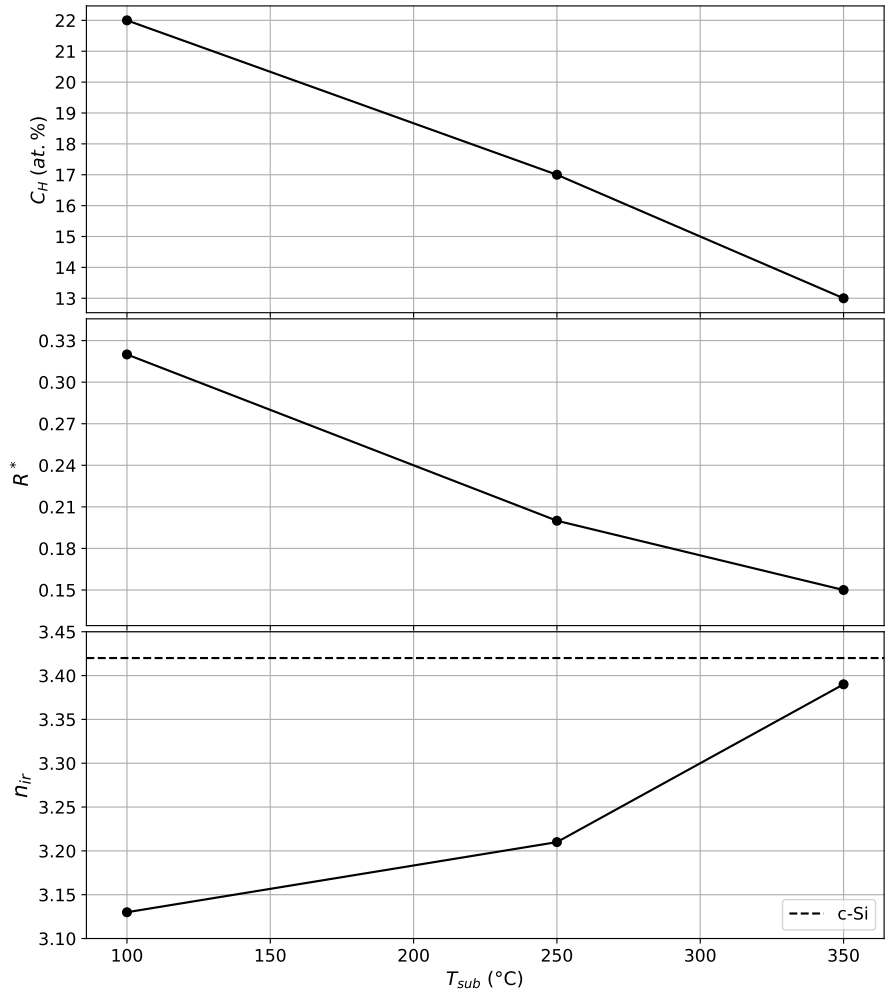

Figure 8: Overview of the a-Si:H FTIR measurement results. The dashed line in the bottom figure denotes the n of c-Si.

T_{sub} (°C)	100	250	350	a-SiC
C_{H} (at.%)	22	17	13	-
R^*	0.32	0.20	0.15	-
n_{ir}	3.13	3.21	3.39	2.63
$n_{\text{ir}}/n_{\text{c-Si,ir}}$	0.91	0.94	0.99	0.77

Table 3: All the FTIR results.

5 RAMAN SPECTROSCOPY

Although our hypothesis is that the dielectric loss is due to voids in the dielectric's network, and not due to the disorder in the network itself, we do not limit ourselves to this view. We retrieve information about the disorder in the network by measuring the bond-angle disorder using Raman spectroscopy. Additionally, from the Raman measurement we can confirm that the a-Si:H is in an amorphous phase.

5.1 MEASUREMENT PRINCIPLE

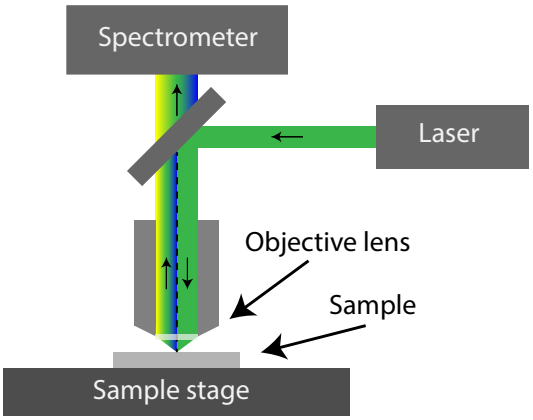

Figure 9: Illustration of the Raman spectroscopic instrument. The sample stage can be moved in three dimensions via an external controller. By moving the stage in the vertical direction, the laser can be focused on the sample.

The Raman instrument works by shining a laser (in our case of 514 nm) at the wafer, and measuring the photons that are Raman scattered in the wafer. Raman scattering is an inelastic process: the photons that come back to the detector are shifted in energy. The total energy remains conserved because the system that we are probing has absorbed or emitted the energy difference by transitioning to a different state.

It is these energy differences that are measured using Raman spectroscopy, and that give us information on the vibrational modes inside the sample. Due to the different interaction mechanism, the Raman spectrum is not the same as the FTIR spectrum, and because of this the method is complementary to FTIR.

5.2 BOND ANGLE-DISORDER

The bond-angle disorder tells us something about the disorder in the a-Si:H network. crystalline silicon has a tetrahedral structure (the four neighbours of a silicon atom lie on the vertices of a pyramid), and in a-Si there is also a tetrahedral structure, but the tetrahedrons do not form a lattice with long-range order.

Additionally, there is also disorder within the tetrahedrons themselves. In c-Si, the tetrahedrons are symmetric, and every bond angle between three silicon atoms is 109.5°. In a-Si the bond angles have a Gaussian distribution around this angle.

The bond-angle disorder $\Delta\theta$ is a measure of this disorder in the silicon bond angles, defined as the root mean square (rms) deviation from the tetrahedral bond angle of 109.5°. It can be measured using Raman spectroscopy [16, 51]:

$$\Delta\theta = \frac{505.5 - \omega}{2.5}, \tag{9}$$

where ω is the center of the a-Si transverse-optic (TO) mode around approximately 480 cm^{-1}. Figures of the measurements that show this mode, and the fitting, are given in the next section. The measured $\Delta\theta$ are given in Section 5.4.

5.3 MEASURED RAMAN SPECTRA AND FITTING

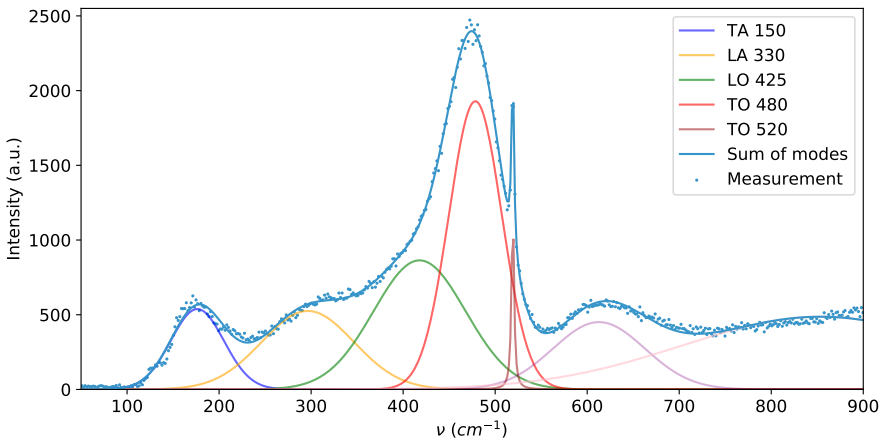

Figure 10: Raman spectrum of the 100 °C a-Si:H film with fitting.

In Fig. 10 we can see the measured Raman spectrum of the 100 °C a-Si:H film. We can clearly see the a-Si TO mode around 480 cm^{-1}. This is the mode from which we calculate $\Delta\theta$.

The fit to the vibrational modes is a sum of Gaussians, and a Lorentzian for the c-Si peak. Around 150 cm^{-1} we can see the a-Si transverse-acoustic (TA) mode, around 330 cm^{-1} the a-Si longitudinal-acoustic (LA) mode, around 425 cm^{-1} the a-Si longitudinal-optic (LO)

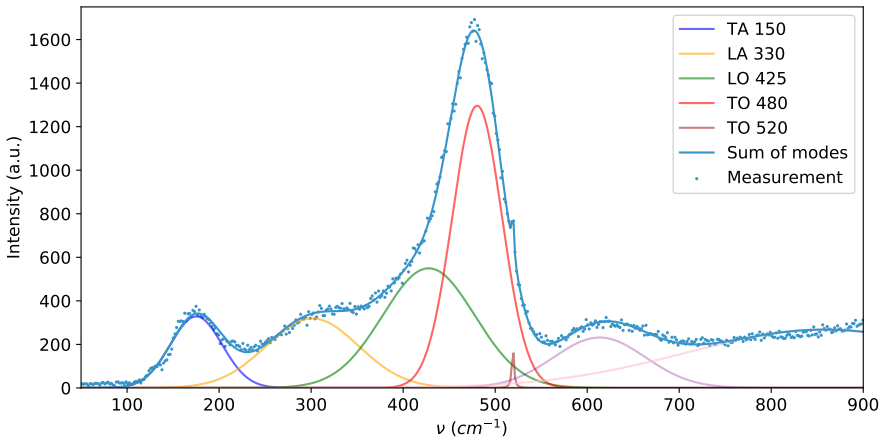

Figure 11: Raman spectrum of the 350 °C a-Si:H film with fitting. The c-Si peak at 520 cm^{-1} is less strong in this spectrum than for the 100 °C and 250 °C a-Si:H films.

mode, and at 520 cm^{-1} the c-Si TO mode. [16, 46, 51]. In Appendix A we conclude that the c-Si peak is due to the c-Si substrate and not due to crystallites inside the a-Si:H.

The Raman signal to the right of the crystalline silicon peak can be attributed to a wide variety of modes. There is an Si-H wagging mode at 640 cm^{-1} [46], and there are the second harmonics 2LA, 2LO and 2TO of the a-Si:H LA, LO and TO modes [30]. For simplicity the signal on the right side is modelled with only two Gaussians.

The c-Si peak at 520 cm^{-1} is less strong in the spectrum of the 350 °C a-Si:H film than in the other two a-Si:H films. This could be due to the higher density of the 350 °C film. The 250 °C spectrum is not shown because it looks very similar to the 100 °C spectrum.

5.4 RESULTS

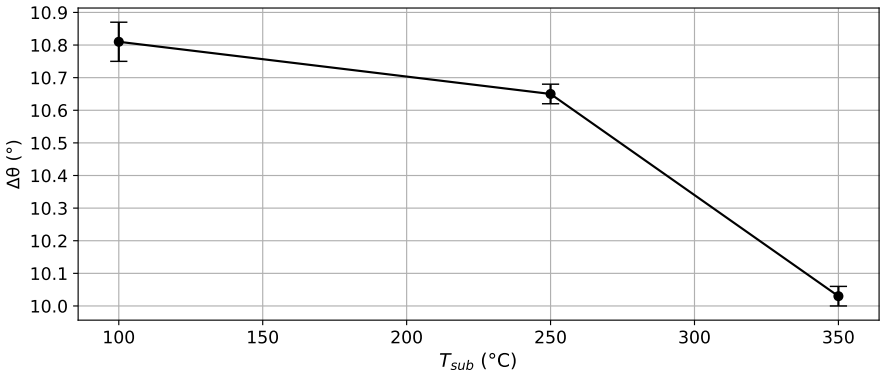

Figure 12: Measured bond angle disorders of the a-Si:H films. The error bars denote the standard deviations that are calculated from the fitting.

The bond-angle disorders that were calculated using Eq. (9) can be seen in Fig. 12 and in Table 4. A monotonic decrease in $\Delta\theta$ is seen with increasing T_{sub}. The errors in the table and in the error bars in the figure are the standard deviations that were calculated from the fits.

T_{sub} (°C)	100	250	350
$\Delta\theta(^\circ)$	10.81 $\pm$ 0.06	10.65 $\pm$ 0.03	10.03 $\pm$ 0.03

Table 4: Measured bond-angle disorder of the a-Si:H films.

6 ELLIPSOMETRY

Using ellipsometry we can measure the void volume fraction (f_v): The fraction of the volume of the dielectric that is filled with voids. Therefore, this measurement helps us in testing our hypothesis that the dielectric loss in a-Si:H stems from voids in the material.

6.1 MEASUREMENT PRINCIPLE

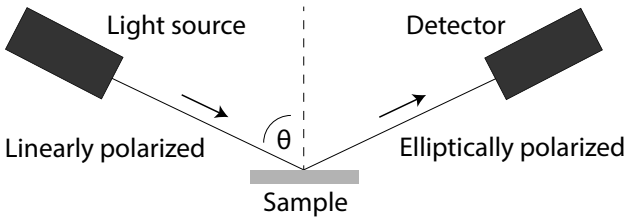

Figure 13: Simplified illustration of an ellipsomery measurement. The measurement is taken at multiple wavelengths and angles of incidence.

Ellipsometry measures the change of the polarization state of the incident light beam that has interacted with the sample. In doing so, it gives us information about the optical constants and thickness of the film. We are using variable angle spectroscopic ellipsometry (VASE): The measurement is not only performed in a range of wavelengths, but also at multiple angles.

Depending on the setup, the incoming light is linearly polarized, and then the polarization state is changed by interaction with the wafer, making it elliptically polarized. The detector contains an analyzer (a polarizer) so that it can measure the change in polarization.

The measured change in polarization is expressed by two real-valued quantities called ψ and Δ that are defined as [58]:

$$\begin{aligned} \tan\psi \cdot e^{i\Delta} &= \frac{r_p}{r_s} \\ &\equiv \rho. \end{aligned} \tag{10}$$

Here r_p and r_s are the reflectivities for s- and p-polarized light, and ρ is just a shorthand notation.

The software CompleteEASE (CE) that is supplied by the manufacturer of the instrument uses the Fresnel equations to calculate $\rho(\theta)$ for a layered structure, where θ is the angle of incidence of the instrument's laser beam. Each layer of the wafer is parametrized by a

thickness t, and relations for $n(\lambda)$ and $k(\lambda)$, where λ is the wavelength of the laser beam. The measurement data is then fitted to the model in CE to find the parameter values.

The a-Si:H wafers that were used for ellipsometry had a 101 nm thermal oxide layer in between the a-Si:H film and the c-Si substrate. The thermal oxide layer increases the difference in refractive index between the film and the substrate, thereby increasing the amount of light that is reflected at the film-substrate interface. Without this thermal oxide layer, ellipsometric measurements of the a-Si:H films were not successful. For the a-SiC film the thermal oxide layer was not necessary.

The measurement was performed at five angles of incidence, ranging from 45° to 75°, in steps of 5°. The wavelength range was 245 to 1688 nm.

6.2 VOID VOLUME FRACTION

The void volume fraction (f_v) is an important quantity for our research, since we are testing the hypothesis that voids are the cause of the dielectric loss in our films. It is defined as:

$$f_v = \frac{V_v}{V}, \tag{11}$$

where V_v is the total volume of voids in the dielectric, and V is the total volume of the dielectric. The Bruggeman effective medium approximation (EMA) can be used to calculate the effective dielectric constant of a binary mixture [35, 47]:

$$f_a \frac{\epsilon_a - \epsilon_{eff}}{\epsilon_a + 2\epsilon_{eff}} + (1 - f_a) \frac{\epsilon_b - \epsilon_{eff}}{\epsilon_b + 2\epsilon_{eff}} = 0, \tag{12}$$

where f_a is the volume fraction of material a, ϵ_a and ϵ_b denote the dielectric constants of materials a and b, and ϵ_{eff} is the effective dielectric constant of the composite material. We model the a-Si as a pure a-Si matrix with voids. In this case f_a is the void volume fraction, ϵ_a is the dielectric constant of a-Si, and ϵ_b is equal to one, the dielectric constant of vacuum.

6.3 ANALYSIS IN COMPLETEEASE

The analysis of the ellipsometry data was performed using CompleteEASE (CE). The layer stack in CE consists of a c-Si substrate (*SI_JAW*), a thin film layer that represents the deposited dielectric, and a surface roughness layer.

In CE a surface roughness layer is always modeled by the Bruggeman EMA, using a volume fraction of 50% voids and 50% of the same material as the underlying layer. Replacing the surface roughness with a native oxide layer (*SIO2_JAW*) in the CE model leads to

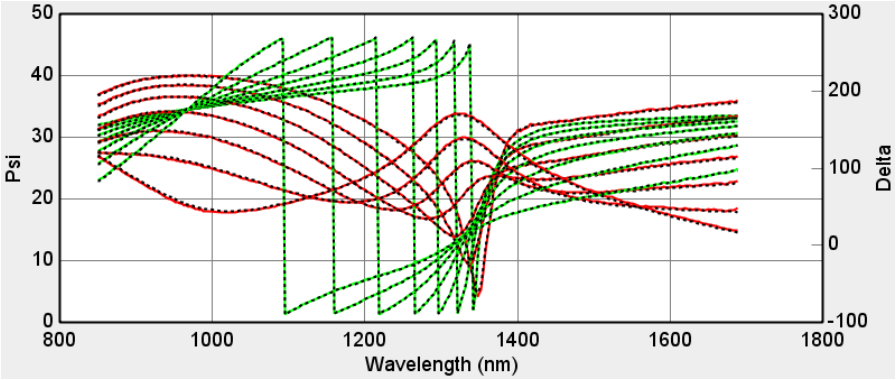

Figure 14: Ellipsometry measurement for the 100 °C a-Si sample. The red curve is the measured ψ and the green curve is the measured Δ. The dashed black curve is the fit to the model.

an increase in f_v of 0.1%. Since this difference is larger than the standard deviation that results from the fit, we have listed 0.1 as the error in Table 5. The MSE is comparable. When using a native oxide layer, this layer fits to 6 nm thickness, even though native oxide stops growing at approximately 2 nm [4]. The surface roughness thickness fits to about 5 nm.

In the case of the a-Si:H films, there is a SiO_2 layer (*SIO2_JAW*) in between the substrate and the a-Si:H layer. The thickness of this layer was set as a free parameter, and the fit result confirms the expected thickness of 101 nm. The deposited films are all modeled as Cody-Lorentz (CL) oscillators.

In the case of a-Si:H, the deposited layer was modeled using the Bruggeman EMA, containing a f_v that is a free parameter in the fitting. In CE this is done by selecting the EMA.mat material. Then, material one can be set to the host material, and material two can be set to void. In this case the host material is set to *a-Si parametrized*, which is just a CL oscillator where all parameters are fixed to literature values. We left all parameters to the standard values.

The a-SiC layer is also modeled as a CL oscillator, but in this case it was necessary to set the parameters *Amp1*, *Br1*, *Eo1*, and *Eg1* to free parameters. The SiC films were not expected to have voids, and indeed an EMA model does not result in a better MSE than the standard CL model.

Fig. 14 shows an example of an ellipsometry measurement on the 100 °C a-Si:H film and the fitting.

6.4 RESULTS

In Fig. 15 and in Table 5 we show the results of the ellipsometry measurements. We see that the f_v of the a-Si:H films decrease monotonically with increasing T_{sub}.

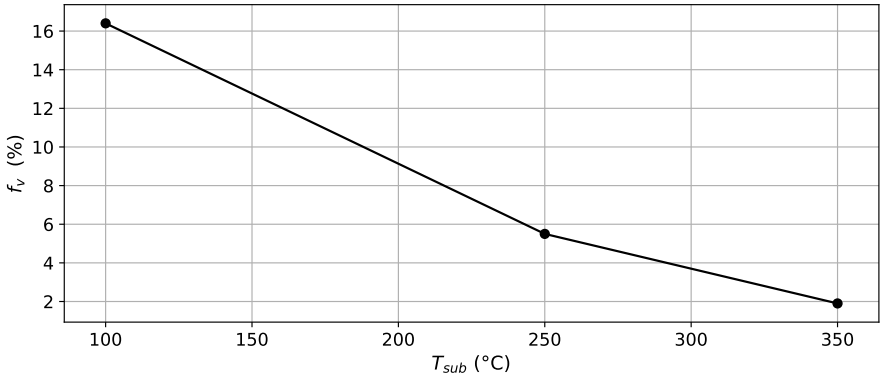

Figure 15: Plot of the measured f_v of a-Si:H.

Material	a-Si 100	a-Si 250	a-Si 350	a-SiC
$f_v(\%)$	16.4 ± 0.1	5.5 ± 0.1	1.9 ± 0.1	-
t (nm)	252.8 ± 0.1	237.4 ± 0.1	261.2 ± 0.2	215.6 ± 0.1
MSE	4.75	3.25	3.96	3.3

Table 5: All the ellipsometry results.

7

DESIGNING A CHIP FOR DIELECTRIC LOSS MEASUREMENTS

Our low-loss dielectrics will find their application in the superconducting resonators of astronomical instruments, and it is these same resonators that serve as excellent loss measurement devices.

As we will see in Chapter 8, the internal quality factor (Q_i) of a resonator, and therefore also its dielectric loss, can be calculated from its $|S_{21}|$ scattering parameter curve as a function of frequency. A vector network analyzer (VNA) is able to do a fast and high resolution microwave (MW) frequency sweep, while simultaneously acquiring the S_{21} data of the circuit with high accuracy. Therefore, the combination of a chip with superconducting resonators and a VNA makes for a very effective loss measurement setup.

7.1 DESIGN CONSIDERATIONS

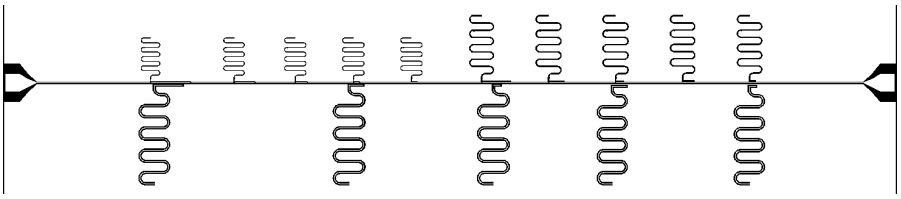

Figure 16: CAD drawing of the 2 cm wide chip. The white regions are Al. In the black regions the Al is patterned away using photolithography, resulting in the dielectric being exposed there. There are 15 quarter-wavelength CPW resonators on the chip. On the left and right side of the chip there are two bonding pads, that are wire-bonded to the coaxial connectors that connect the chip to the VNA. The empty parts on the top and bottom of the square chip are not shown.

7.1.1 *A microwave chip with coplanar waveguides*

In the introduction of this thesis we have mentioned that this research is motivated by the application of the dielectrics in microstrip-based mm/sub-mm (MMW) circuit elements. Here we want to point out that for our chip we are using quarter-wavelength CPWs, and we are measuring the microwave (MW), i.e. at a few GHz, dielectric loss.

We have chosen to make use of CPWs instead of microstrips because a CPW chip allows for faster fabrication. A microstrip is not necessary to measure the dielectric loss. We designed a chip for mea-

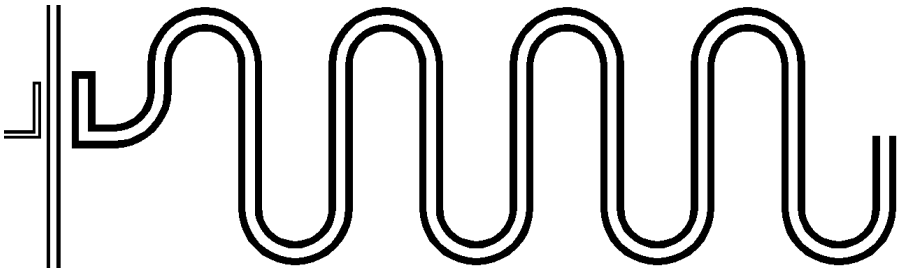

Figure 17: Close-up of the CAD drawing of one of the quarter-wavelength CPW resonators. In addition to the resonator, on the left we can see the readout line, and the coupler of another resonator. The width of this image corresponds to approximately 2.2 mm on the chip.

suring the the MW loss, and not the MMW loss, because the MW measurements were easier to perform than the MMW measurements. It is expected that the MW loss is a strong indication of the MMW loss, since from TLS theory we expect a constant density of TLS states in the energy domain [38, 54]. We also note that the MW losses are interesting for the development of microstrip-based MKIDs [29]

The CPWs on this chip are made of aluminium (Al). In comparison with niobium titanium nitride (NbTiN), Al does not have the problem of over-etching into the substrate, resulting in more reliable filling fraction calculations. Al does have a lower critical temperature (T_c) than NbTiN, but this is not expected to cause significant ohmic losses since the chip will be used at 120 mK, well below the T_c of 1.2 K of Al. The patterning of the Al was done using photolithography by the Netherlands Institute for Space Research (SRON) in Utrecht.

7.1.2 *A range of Q_c and a range of geometries*

Our measurement of $|S_{21}|$ is the most sensitive to Q_i when Q_i is close to the coupling quality factor (Q_c). One way to see this is to note that the minimum of the resonance dip ($S_{21,min}$) is equal to

$$S_{21,min} = \frac{1}{1 + \frac{Q_i}{Q_c}}, \tag{13}$$

and therefore when Q_i gets relatively large, the dip becomes too deep to be accurately measured, and when Q_c gets relatively large the dip becomes too shallow and is too strongly influenced by the background signal.

Since beforehand we did not know the dielectric losses of our deposited dielectrics, we had to make the chip sensitive to a wide range of losses. Therefore we are using resonators with five different Q_c: 3000 (3k), 10k, 30k, 100k and 300k.

The dielectric loss of superconducting resonators is known to not only come from the bulk of the dielectric, but also from TLS on the

resonator's surface [2, 15, 56, 57]. The geometry of the CPW influences how strongly the surface TLS affect its Q_i. A smaller CPW will have more of its electric field's energy concentrated in the vicinity of the resonator's surface. Therefore, a small CPW more strongly probes the surface TLS than a larger CPW.

Being able to, at least qualitatively, see a difference between the bulk and the surface losses is a reason that our chip design has three different CPW geometries. Additionally, the radiation losses of a CPW are also dependent on its geometry [12]. Acquiring data with multiple CPW geometries gives us more insight in the various loss mechanisms that are contributing to $1/Q_i$.

Finally, we point out that the 15 resonators each have a different MW frequency (F_r), so that their resonance dips are separated and we can easily identify the individual resonators from their F_r.

7.2 SIMULATING THE COUPLERS

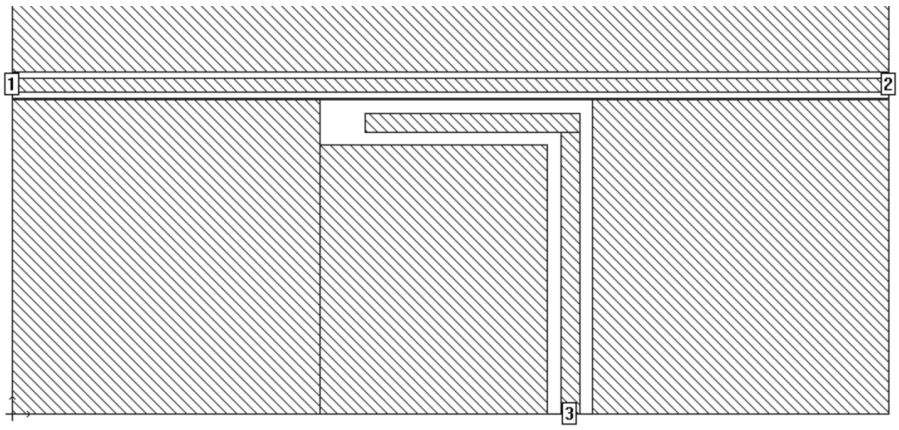

Figure 18: Coupler simulation in Sonnet. The numbers denote the port numbers. The coupler length (horizontal section of the coupler) is parametrized. The top part of the ground plane is not shown, it is symmetric around the throughline.

As we have explained in Section 7.1.2, we want to have resonators with five different coupling quality factors. The resonator is coupled to the readout line with a so-called elbow coupler. A schematic of such a coupler can be seen in Fig. 18.

The length of the part of the coupler that runs parallel to the readout line is the coupler length l_c. Since Q_c quantifies the coupling of the resonator to the readout line, it makes sense that it influenced by l_c and by the coupler's distance to the readout line.

We have simulated a range of coupler lengths in Sonnet, a commercial high frequency EM solver. From the Sonnet simulation we get S_{13}, from which Q_c can be calculated using Eq. (14). By interpolating the Sonnet results, we calculate the l_c that are required to reach the

desired Q_c. Below we give the equation that we used to calculate Q_c from S_{13}: [28].

$$Q_c = 2\pi \frac{\text{energy stored in the resonator}}{\text{energy leaked per cycle to ports 1 and 2 from port 3}} = \frac{\pi}{2|S_{13}|^2}. \quad (14)$$

7.3 SENSITIVITY TO THE DIELECTRIC LOSS IN THE FILM

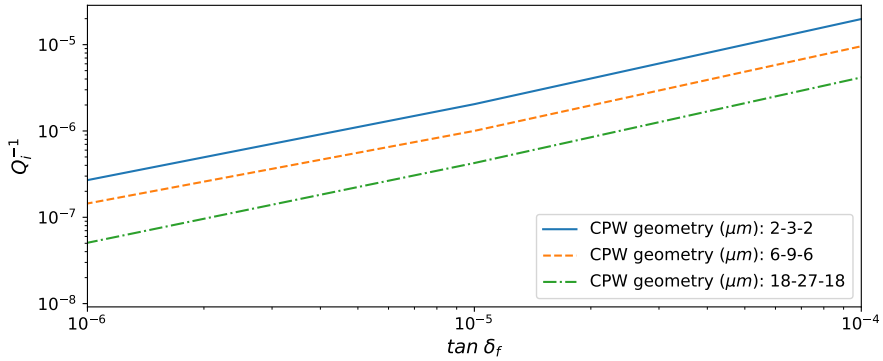

Figure 19: Simulation of $1/Q_i$ in Sonnet for a range of $\tan\delta_f$ for a 250 nm thick film with a dielectric constant of 10, at 5 GHz.

To check whether the $1/Q_i$ of the CPW resonator is sensitive enough to the dielectric loss tangents ($\tan\delta_f$) of the approximately 250 nm thick films, we have simulated a two-port CPW in Sonnet for a range of loss tangents and for each CPW geometry. For the dielectric constant of the film in this simulation we have used the value 10. We can see the results of the simulations in Fig. 19.

We can see that the $1/Q_i$ of the smallest CPW geometry is the most sensitive to changes in $\tan\delta_f$. This is because for this geometry the largest portion of the electric field's energy is inside the film. From this figure we can conclude that with our resonators we can measure the $\tan\delta_f$ as low as order 10^{-6} for 250 nm thick films. Thicker films will only result in more accurate measurements since a larger portion of the electric field's energy is then inside the film.

8

DIELECTRIC LOSS MEASUREMENTS

In this chapter we come to the final step of testing our hypothesis: Measuring the dielectric losses of the deposited films. Before we come to the results, in the first section we explain the measurement principle, and we show the calculation of the filling fractions in Sonnet.

Then we come to the measurement results. First, we show the measured $1/Q_i$. Because only part of the electric field's energy is inside the film, this is not yet the loss tangent of the film ($\tan\delta_f$) that we want to obtain. Using the calculated filling fractions, we then come at an upper limit of $\tan\delta_f$. Finally, using a reference measurement on a c-Si chip, we come at an estimation of $\tan\delta_f$.

8.1 MEASUREMENT PRINCIPLE

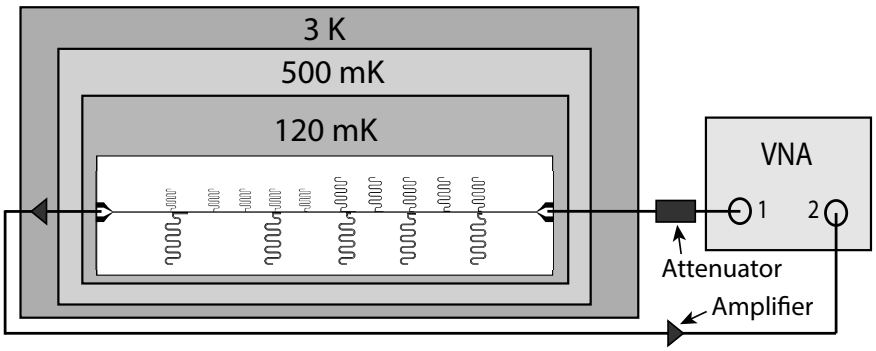

Figure 20: Simplified illustration of the loss measurement setup.

The quantity that we are measuring, from which we calculate the quality factors of the resonator, is the scattering parameter $S_{21}(f)$, as a function of MW frequency. In Fig. 21 we can see a plot of a measured resonance dip: The plot shows the magnitude of $S_{21}(f)$ for a resonator with a resonance frequency of approximately 4.26 GHz.

It is from the shape of this resonance dip that we obtain the quality factors, as is explained in Section 8.1. Since all resonators have their own resonance frequency, we can identify which resonance dip belongs to which resonator.

A vector network analyzer (VNA) is used to measure the scattering parameter $S_{21}(f)$. The VNA generates a MW signal at port 1, that is connected to one end of the readout line of our chip, and measures the amplitude and phase of the signal at port 2, that is connected to the other end of the readout line of the chip. A simplified version of the setup is drawn in Fig. 20.

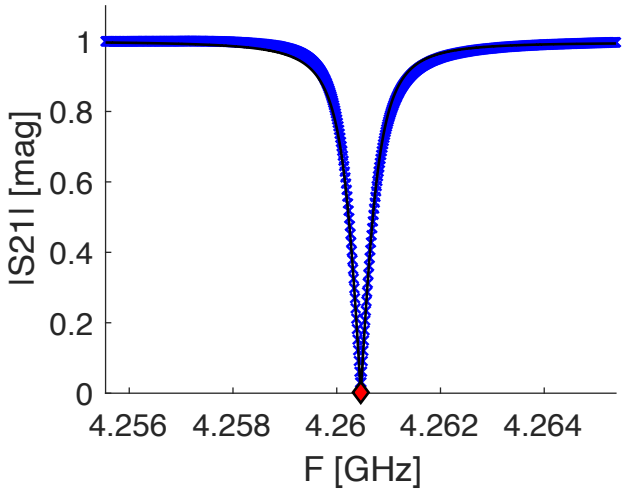

Figure 21: Example of a measured resonance dip.

Because we want to study the MW loss at cryogenic temperatures, and because we need the Al of our chip to be superconducting, the chip is placed inside an adiabatic demagnetization refrigerator (ADR) that cools it down to 120 mK. This is approximately 10% of the T_c of the Al. The readout signal is attenuated before going to the chip, to realize low readout powers. The readout signal that goes from the chip to the VNA is amplified using two amplifiers, one at the 3K stage and one at room temperature [52].

Obtaining the quality factors by fitting

By fitting the $S_{21}(f)$ measurements that we described in the previous section to the squared Lorentzian in Eq. (15), we can determine the loaded quality factor (Q), f_r and $S_{21,\min}$, and from this also Q_i and Q_c:

$$|S_{21}|^2 = \left(1 - \frac{(1 - S_{21,\min}^2)}{1 + (2Q\frac{f - f_r}{f_r})^2}\right) A(f). \tag{15}$$

$$Q_i = \frac{Q}{S_{21,\min}}. \tag{16}$$

$$Q_c = \frac{Q_i Q}{Q_i - Q}. \tag{17}$$

$S_{21,\min}$ is the depth of the resonance dip, and $A(f)$ is a linear background slope, which is fitted separately.

8.2 CALCULATING THE FILLING FRACTIONS

The filling fraction (p) is defined as the fraction of the resonator's electric field's energy that is inside the dielectric film [14]. This parame-

ter determines how strongly the resonator is affected by the dielectric loss of the film:

$$\frac{1}{Q_i}(g) = p_f(g) \tan\delta_f + b(g), \tag{18}$$

where Q_i denotes the measured Q_i of the resonator, the subscript f denotes the film, $\tan\delta_f$ denotes the loss tangent of the film, and b denotes the sum of all losses other than the film's loss tangent. These are radiation losses, surface losses, and ohmic losses.

The variable g denotes a geometry factor to make the dependence on the CPW geometry explicit. The filling fraction and the other losses are both dependent on the CPW geometry, but $\tan\delta_f$ is not since this is an intrinsic property of the dielectric material. However, it is dependent on the temperature and the electric field inside the dielectric [14].

We use Sonnet for calculating the filling fractions for each dielectric film and each CPW geometry. As we can see from Eq. (18), by simulating $1/Q_i$ and only varying $\tan\delta_f$, the slope of $1/Q_i$ versus $\tan\delta_f$ is equal to p_f.

In Fig. 22 we show as an example the simulation of the 250 °C a-Si:H film. As expected, in this figure we can see that smaller CPW geometries have steeper slopes, and therefore larger p_f.

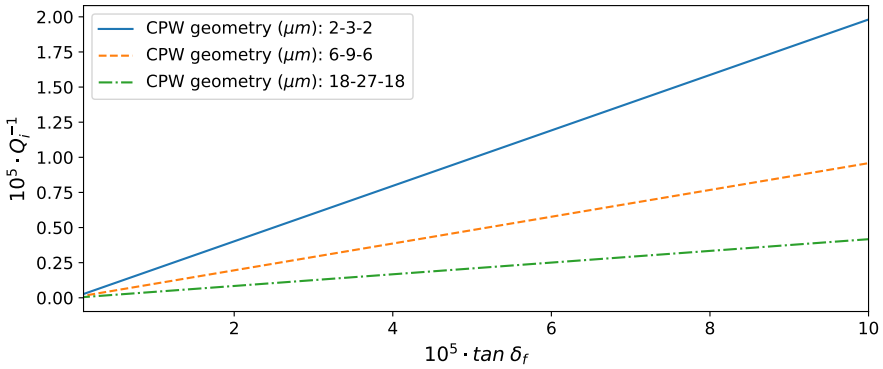

Figure 22: Example of the Sonnet simulation results of the Q_i of the 250 °C film, that is used to calculate the filling fractions of this film.

In these simulations we use the film thicknesses as measured with ellipsometry, listed in Table 5, and MW dielectric constants that were estimated using the measured IR dielectric constants, as is explained in Appendix C. In this way we get the filling fractions that are listed in Table 6.

As a sanity check we calculate the p_f of the c-Si chip analytically. In Sonnet, metal layers do not have a thickness. Therefore the electric field is equal above and below the substrate surface. In this case we can simply calculate the filling fraction as:

$$p_{\text{sub,c-Si}} = \frac{\epsilon_{\text{si,mw}}}{\epsilon_{\text{si,mw}} + \epsilon_{\text{vacuum}}} = \frac{11.44}{11.44 + 1} = 0.920, \tag{19}$$

	2-3-2	6-9-6	18-27-18
c-Si	0.920	0.920	0.920
a-Si 100	0.208	0.101	0.044
a-Si 250	0.197	0.095	0.042
a-Si 350	0.214	0.103	0.045
a-Si a-SiC	0.193	0.095	0.042

Table 6: Calculated filling fractions of the dielectric films, and of the c-Si substrate for the reference wafer. Calculations were performed in Sonnet.

which is the same value as calculated in Sonnet.

8.3 RESULTS

Now that we have calculated the filling fractions that we need for calculating $\tan\delta_f$ from the Q_i measurements, we are ready to discuss the dielectric loss measurements. We note that in the following figures the $1/Q_i$ are plotted as a function of the internal resonator power (P_{int}).

Since the TLS induced loss tangent is influenced by the electric field inside the dielectric, the internal resonator power is more insightful than the readout power, although knowledge of the electric field strength inside the dielectric would be preferred. However, for CPWs this is difficult due to the non-homogeneous field. P_{int} can be calculated from the read-out power [14]:

$$P_{int} = \frac{2}{\pi}\frac{Q^2}{Q_c}P_{read}. \tag{20}$$

Because the Q_i turned out to be very good, we have decided to use the resonators with the largest Q_c for measuring Q_i, since these are able to most accurately measure such high Q_i, as was explained in Section 7.1.2.

Finally we note that in this section we use the notation 2-3-2, etc. to refer to a CPW with a 2 µm slot width and a 3 µm center line width.

8.3.1 *Measured internal quality factors*

In Fig. 23 we see the measurement results of the resonator's $1/Q_i$ for all materials and CPW widths. We can see that the $1/Q_i$ is larger for the smallest CPW geometry. This may hint at surface losses, because the filling fraction of the surface increases when the CPW becomes smaller.

We can also see that for the smallest CPW width, at approximately -40 dBm P_{int} the $1/Q_i$ of the chips with deposited films are lower

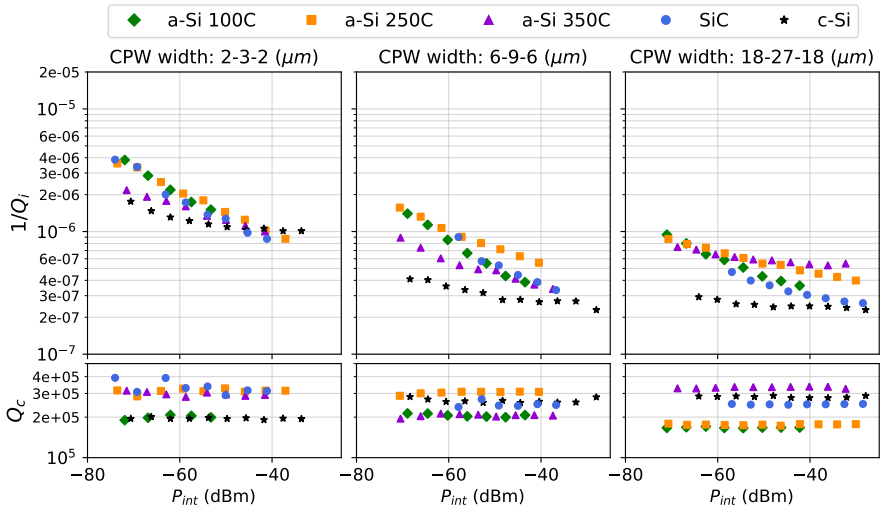

Figure 23: $1/Q_\mathrm{i}$ and Q_c.

than the $1/Q_\mathrm{i}$ of the c-Si reference. This might be an indication that these data points do not differ significantly in comparison with the measurement error. It could also mean that the surface losses on the c-Si chip are relatively large, although as far as we know there is no explanation to support this. The fitting errors of $1/Q_\mathrm{i}$ are on the order of 10^{-8}.

8.3.2 *An upper limit for the loss tangent*

For testing our hypothesis, we do not need the $1/Q_\mathrm{i}$ of the resonator, but the $\tan\delta_\mathrm{f}$ of the dielectric film. In this section we calculate the upper limits of the $\tan\delta_\mathrm{f}$ of the films and of the c-Si substrate. The upper limits of $\tan\delta_\mathrm{f}$ are a valuable piece of information: We know that the films are at least better than this. We can see from Eq. (18) that we can express $\tan\delta_\mathrm{f}$ as

$$\tan\delta_\mathrm{f} = \frac{\frac{1}{Q_\mathrm{i}}(g) - b(g)}{p_\mathrm{f}(g)}, \tag{21}$$

where $b(g)$ is the sum of all other losses apart from the loss tangents. If we do not know $b(g)$, setting it to zero provides us with an upper limit for $\tan\delta_\mathrm{f}$. The results of this calculation are plotted in Fig. 24.

We can see that the upper limit calculations for the 2-3-2 and 6-9-6 CPW geometries agree well, but that the 18-27-18 CPW geometry has larger upper limits. Since we are talking about the upper limit of $\tan\delta_\mathrm{f}$, which is independent of the CPW geometry, we can take the lowest measured value as the upper limit.

In other words, it might be that the 18-27-18 CPWs suffer more losses apart from $\tan\delta_\mathrm{f}$ than the smaller CPWs. This could for example be due to radiation loss, which is larger for larger CPWs [12].

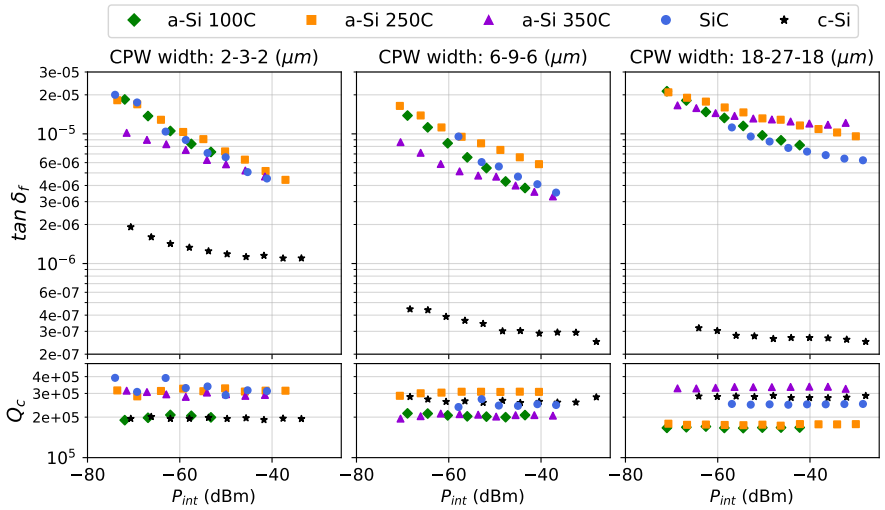

Figure 24: Upper limits of $\tan\delta_{\mathrm{f}}$.

Based on the upper limit calculation, we conclude that all four films have an excellent loss tangent below 10^{-5} at -50 dBm internal resonator power and 120 mK.

At the lowest measured P_{int}, where the effect of the TLS is the strongest, we can see that the upper limit of the $\tan\delta_{\mathrm{f}}$ of the 350 °C a-Si:H film is a factor two lower than for the other films. We emphasize that this does not mean that the 350 °C a-Si:H film is superior, by definition we can not draw this conclusion from an upper limit calculation.

Since the differences between the dielectric losses of the films are expected to increase at lower P_{int}, it would be interesting to measure lower powers to investigate the differences in TLS densities between the films.

We can see that the upper limit of the c-Si drops rapidly when going from the 2-3-2 to the 6-9-6 CPW geometry. Again, this might point to a large contribution of surface losses for the c-Si chip.

8.3.3 *An estimation of the loss tangents*

As we said, the upper limits of $\tan\delta_{\mathrm{f}}$ are a valuable piece of information. However, they are not conclusive enough for testing our hypothesis. To calculate the values of $\tan\delta_{\mathrm{f}}$ we have to know $b(g)$. It is expected that $b(g)$ could be due to surface TLS, loss inside the substrate, radiation loss, and ohmic loss.

Estimating that the radiation and surface losses of the c-Si chip might be similar to these losses for the other chips, as an estimation for b(g) we consider it to be equal to the $1/Q_{\text{i}}$ of the c-Si chip:

$$\begin{aligned} b(g) &\approx \frac{1}{Q_{\text{i,c-Si}}} \\ &= p_{\text{sub,c-Si}} \tan\delta_{\text{c-Si}} + \sum_{\text{j}} p_{\text{s,j}}(g) \tan\delta_{\text{s,i}} + \frac{1}{Q_{\text{radiation}}}(g) \end{aligned} \tag{22}$$

Here $p_{\text{sub,c-Si}}$ is the filling fraction of the substrate of the c-Si chip, which is 0.92, as we know from Table 6. The $\tan\delta_{\text{s,j}}$ denote different kinds of possible surface loss contributions on the c-Si chip, and the last term denotes the radiation loss of the c-Si chip. This estimation is expected to deviate from the true value of $b(g)$ for two reasons.

Firstly, we know for a fact that $p_{sub}(g)$ of the films is different than $p_{\text{sub,c-Si}}$. This is because part of the electric field's energy that is in the substrate on the c-Si chip, is in the thin film on the other chips. However, if $\tan\delta_{\text{c-Si}}$ would be sufficiently small, this would have little effect on the estimation.

Secondly, the loss contributions other than the substrate loss are not necessarily the same. It might for example be that there is a different kind of lossy surface for each chip. Keeping these limitations of this estimation in mind, we show the results of the calculation in Fig. 25:

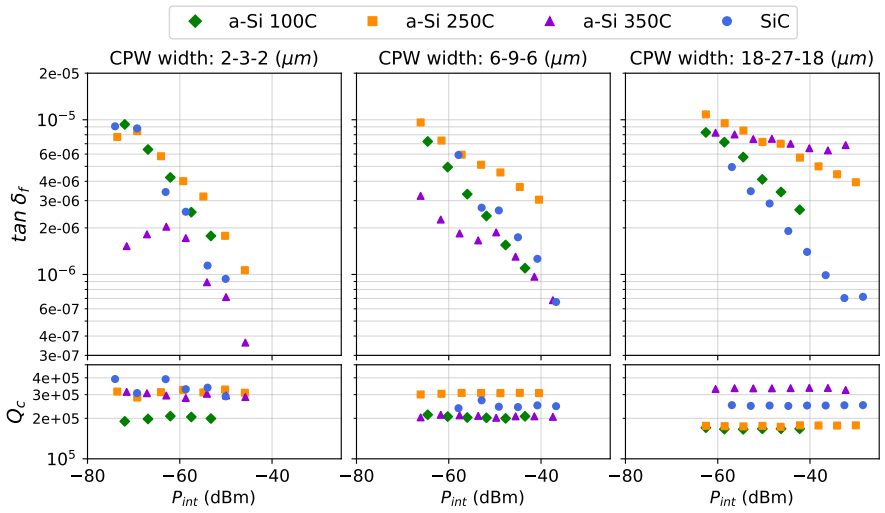

Figure 25: Estimation of the $\tan\delta_{\text{f}}$ of the films.

First we note that the c-Si values are not shown, because we cannot use the c-Si chip as its own reference. We can see that in this estimation, for the smallest CPW geometry and at low P_{int}, the 350 °C a-Si:H film performs better than the other films. At the largest CPW geometry this is not the case.

However, here it must be said that for this geometry the measured P_{int} were not as low as for the smallest geometry, and it is at the

low powers that the differences between the films are expected to be the most significant. Still, this is only an estimation of $\tan\delta_f$ and based on this estimation we cannot draw a conclusion on the possible superiority of a film.

9 CONCLUSION

Our hypothesis was that the dielectric in a-Si:H stems from voids in the material, and that it can be reduced by depositing at high substrate temperatures (T_{sub}). The FTIR, Raman, and ellipsometry results show that the hydrogen content, microstructure parameter, bond angle disorder and void volume fraction of a-Si:H all decrease monotonically with increasing T_{sub}. The IR refractive index approaches the value of c-Si for at a T_{sub} of 350 °C.

Interestingly, we do not see a correlation of the room temperature results with the dielectric losses: All four films have an excellent microwave (MW) loss tangent below 10^{-5} at 120 mK and -50 dBm internal resonator power.

We cannot form a definitive conclusion about our hypothesis, since we only know the upper limits of the dielectric loss tangents, and since we do not know the magnitude of the electric field inside the dielectric. More research on the dielectric losses is recommended, for example using microstrip lines or lumped element parallel plate capacitors.

On a practical note, the 350 °C a-Si films have the problem that all films deposited at this temperature had blisters. A practical benefit of both the a-SiC and the 250 °C a-Si films is that they have almost zero stress.

We conclude by saying that the low dielectric losses make these films promising for application in MW kinetic inductance detectors and mm/sub-mm (MMW) on-chip filters. These promising results will likely lead to the application of one of the dielectrics in DESHIMA 2.0.

9.1 RECOMMENDATIONS FOR FUTURE WORK

In order to draw stronger conclusions on the hypothesis, a more extensive analysis of the current data could be made. This requires calculating the electric field distribution around the CPW, for example using COMSOL. Also, the radiation loss and ohmic losses should be calculated.

Loss measurements with microstrips or lumped element parallel plate capacitors would provide more clarifying results. The electric field distribution inside the dielectric would be more homogeneous than when using CPWs, and this is very helpful in the analysis because the electric field strength inside the dielectric is what influences the TLS induced loss tangent.

We recommend measuring the MMW losses: It will be interesting to know if the excellent dielectric losses also hold for these wavelengths. Firstly, this is important knowledge for the application of the dielectrics in the MMW circuit elements, and secondly it is interesting from a scientific point of view to test the constant energy density of states of the TLS.

It would be very interesting to measure the loss tangent of e-beam evaporated a-Si without hydrogen, to test the superiority of PECVD a-Si:H and the role of hydrogen and its passivation of dangling bonds. A study on the the substrate temperature dependence of the dielectric loss for e-beam a-Si would also lead to an interesting comparison with the internal friction measurements by Liu et al. [26]. The Kavli Nanolab cleanroom at TU Delft has recently acquired a new e-beam evaporator, possibly with a substrate heater.

Regarding the measurement of the hydrogen content and microstructure parameter, we have noticed that there has been a study on the measurement of these parameters using Raman spectroscopy [53]. The authors of this paper have determined the ratios of the Raman scattering cross sections for Si-H to Si-Si bonds and for SiH_2 to Si-Si bonds. It is certainly worthwhile to look into this method, because this would enable the measurement of $\Delta\theta$, R^*, C_H and the amorphicity in a single measurement.

The FTIR analysis could be further improved by making the TMM calculation Kramers-Kronig consistent [18]. This could improve the fitting at the edges of the absorption spectra. Also, measuring on single-side polished wafers could be reconsidered, since this is less expensive. For this a comparison could be made of the results of a measurement on a SSP and a DSP wafer. It is also possible to model the scattering of the wafer in a generalized TMM that models surface roughness [20].

For the ellipsometry measurements it would be interesting to analyze the imaginary part of the dielectric constant, which can give additional information about the film's microstructure and about its amorphicity [9]. It would also be interesting to use transmission electron microscopy (TEM) or x-ray diffraction to further investigate the amorphicity of the films.

Finally, a more complete characterization of the SiC film by also analyzing it with FTIR and Raman spectroscopy would be interesting, giving us information about its network disorder and composition [19, 32, 42].

A

AMORPHICITY OF THE A-SI:H FILMS

In this appendix we discuss the measurements that we have done to confirm that the a-Si:H films are amorphous.

Depending on the deposition details, silicon produced by PECVD can occur in various phases: amorphous (a-Si), nano-crystalline (nc-Si) or micro-crystalline (μc-Si), and poly-crystalline silicon (poly-Si). a-Si is completely amorphous, and contains no crystalline grains (crystallites). The names nc-Si and μc-Si are sometimes used interchangeably, or sometimes the names differentiate between the average grain size. If the μc-Si reaches a very large crystalline volume fraction, it is often referred to as poly-Si. It is possible for the Raman laser to

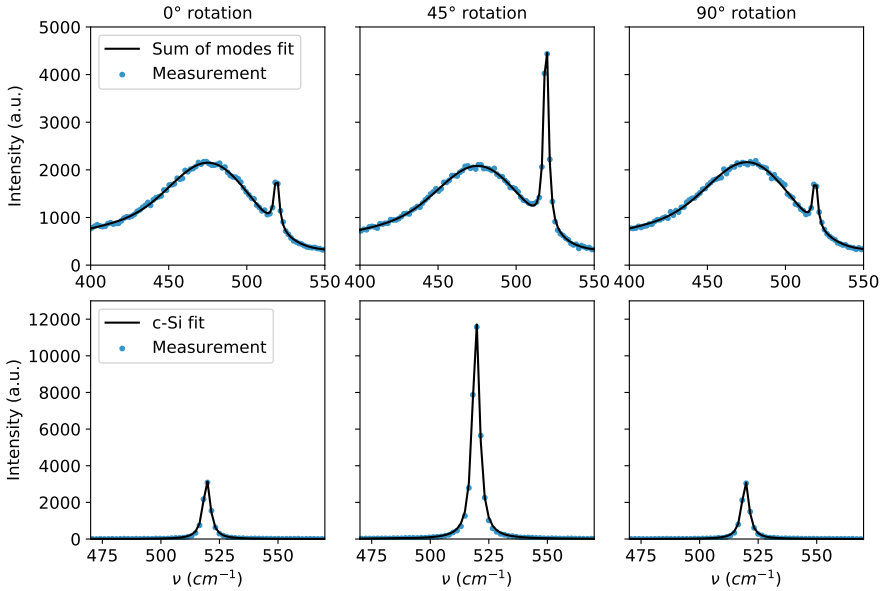

Figure 26: Raman measurements of the 237.4 nm thick a-Si:H film that was deposited at 250 °C. The 100 °C and the 350 °C films show a similar oscillating behavior.

locally crystallize the sample [23]. It is confirmed that the Raman measurements at a 5% laser power do not crystallize the sample in two ways: first by measuring each film at only 0.5% of the laser power, which is well below the instrument's recommended value of 5%. Next to this we observe that the thicker films, that do not have the c-Si peak, also do not show this peak at 5% laser power.

It has been found that for the films with approximately 250 nm thickness, a c-Si peak from the substrate is present in the Raman signal. There are two qualitative observations that make us conclude that this peak comes from the substrate:

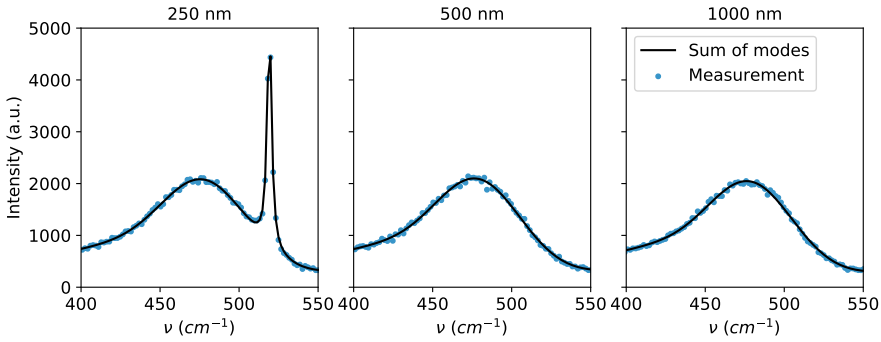

Figure 27: Raman measurements of a-Si:H films with three different thicknesses, all deposited at 250 °C.

Firstly, as can be seen in Fig. 26, the c-Si peak's intensity is dependent on the rotation of the wafer around the axis orthogonal to it's surface (<100> direction). The stated angles are only approximate, angles were measured with a simple ruler. The peak intensity is minimal when the wafer is positioned with the flat that denotes the <110> direction, at a 0° angle. It reaches a maximum at a 45° angle, and again reaches the minimum at a 90° angle. A reference measurement of the substrate leads to comparable results. If the crystalline peak would be due to nano-crystalline particles in the a-Si film, then this oscillating behavior of the peak intensity with wafer rotation is not expected, because the nano-crystalline particles would be randomly oriented inside the amorphous silicon matrix.

The second argument relates to Fig. 27: we can see that the c-Si peak is only present for the films with the lower thickness of approximately 250 nm, and not for films of 500 and 1000 nm thickness that were deposited with the same deposition parameters. If the peak would come from nano-crystalline particles in the a-Si layer, then this would mean that there is either a thickness dependence on the resulting phase of the entire a-Si layer, or else that there is a phase gradient in the <100> direction of the a-Si layer. As far as we know, this is not expected to be true. The two arguments combined lead us to conclude that the films are fully amorphous. Transmission electron microscopy (TEM) or x-ray diffraction could be used to validate this [41].

B

DETAILS ON THE TMM MODELING OF THE SUBSTRATE

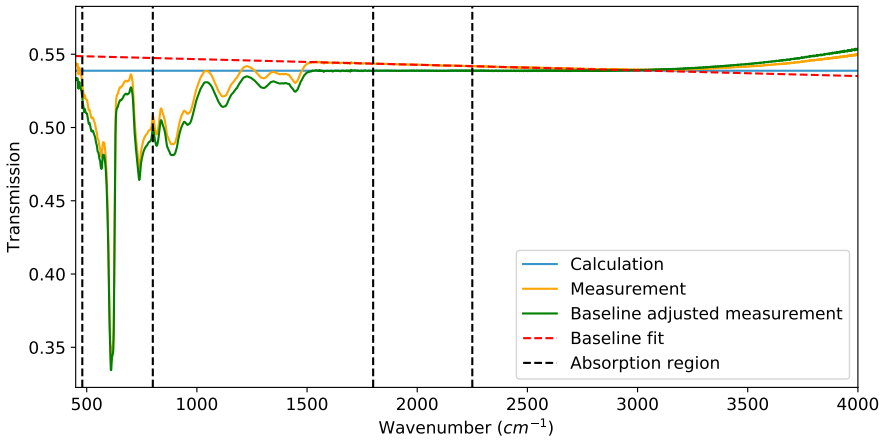

Figure 28: FTIR baseline adjustment for the c-Si substrate. The largest adjustment is below 2% of the measured transmission.

In this appendix we discuss more details about the modeling of the substrate in the TMM calculation for FTIR, mainly a baseline adjustment of at most 2% of the transmission that was required to make make the baseline transmission (transmission in non-absorption regions) horizontal.

As can be seen in Fig. 28, the substrate has a non-horizontal baseline transmission. This is not an effect due to the measurement apparatus itself, since a measurement with an empty sample holder results in a horizontal transmission. It has been excluded that the native oxide has an influence on the transmission, by performing an additional measurement after an HF dip, which removes the native oxide. The negative slope below 3000 cm^{-1} may hint at scattering, although this does not explain the positive curved slope at higher frequencies. Also, the substrate is double-side-polished (DSP), and because of this scattering effects due to surface roughness are expected to be negligible.

Because the origin of the non-horizontal baseline is at this moment not understood, we address this problem by making a baseline adjustment to the measurement data. The adjustment is always below 2% of the measurement, and it is done in a reproducible way by fitting a straight line to the measurement data in the non-absorbing region from 1600 to 2500 cm^{-1}.

When using a single-side-polished (SSP) substrate, the transmission baseline decreases strongly with increasing wavenumber, to less than 25% transmission at 4000 cm^{-1}, as can be seen in Fig. 29. This

is due to scattering caused by surface roughness on the unpolished side. The transmission slope is approximately linear in wavenumber below 2500 cm^{-1}. A curvature of the slope can be seen at the largest wavenumbers. It might be the case that this has the same origin as the curvature that can be seen in Fig. 28 for the DSP substrate.

Both the DSP and SSP wafers that are shown were fabricated using the CZ process. The measured SSP wafer is an n-type wafer with a resistivity of 1-5 Ω cm, and the measured DSP wafer is a p-type wafer with a resistivity larger than 1 kΩ cm.

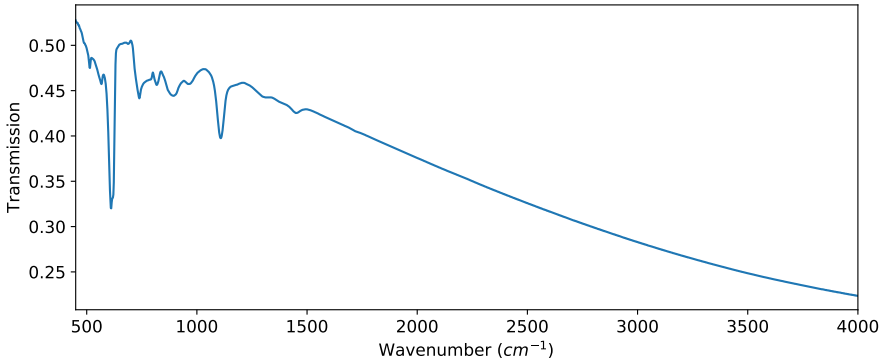

Figure 29: FTIR transmission of an SSP wafer.

C

ESTIMATING THE MICROWAVE DIELECTRIC CONSTANTS

To approximate the microwave (MW) dielectric constants ϵ_{mw} of the films, we make use if the infrared (IR) dielectric constants that we measured using FTIR. The dielectric constant of c-Si in the IR frequency band is 11.70, compared to 11.44 in the MW frequency range. We estimate the ϵ_{mw} as follows:

$$\epsilon_{\mathrm{mw}} \approx \left(\frac{n_{\mathrm{ir}}}{n_{\mathrm{si,ir}}} \right)^2 \cdot \epsilon_{\mathrm{si,mw}}. \tag{23}$$

This results in the following dielectric constants:

Material	a-Si 100	a-Si 250	a-Si 350	a-SiC
ϵ_{mw}	9.5	10.1	11.2	6.8

Table 7: MW dielectric constants estimated from IR dielectric constants.

D

SKEWED RESONANCE DIPS

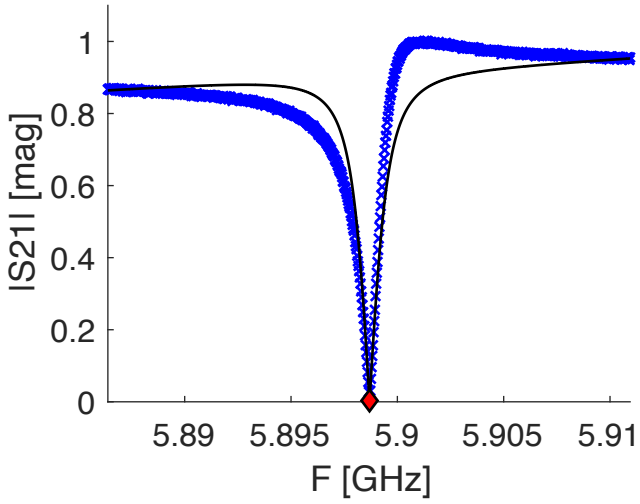

Figure 30: Example of a measured skewed resonance dip.

Some of the measured resonance dips are skewed, in Fig. 30 we can see an example of such a skewed resonance dip. The fitting of $|S_{21}|^2$ that was explained in Section 8.1 does not take this skewedness into account. There are skewed Lorentzian fitting methods that do take this skewedness into account [14].

E

ALL MEASUREMENT RESULTS

Material	a-Si 100	a-Si 250	a-Si 350	a-SiC
T_{sub} (°C)	100	250	350	400
$\tan\delta$	$< 10^{-5}$	$< 10^{-5}$	$< 10^{-5}$	$< 10^{-5}$
C_H (at.%)	22	17	13	-
R^*	0.32	0.20	0.15	-
n_{ir}	3.13	3.21	3.39	2.63
$n_{ir}/n_{c\text{-}Si,ir}$	0.91	0.94	0.99	0.77
$\Delta\theta$	10.81 ± 0.06	10.65 ± 0.03	10.03 ± 0.03	-
f_v (%)	16.4 ± 0.1	5.5 ± 0.1	1.9 ± 0.1	-
σ (MPa)(tens.)	128.7	3.0	-379.0	-19.6

Table 8: The loss tangents are the upper limits of the microwave loss tangents, measured at 120 mK and -50 dBm internal resonator power.

BIBLIOGRAPHY

[1] Maria Rosa Ardigo, Maher Ahmed, and Aurélien Besnard. "Stoney formula: Investigation of curvature measurements by optical profilometer." In: *Advanced Materials Research* 996 (2014), pp. 361–366. ISSN: 16628985. DOI: 10.4028/www.scientific.net/AMR.996.361.

[2] R. Barends et al. "Reduced frequency noise in superconducting resonators." In: *Applied Physics Letters* 97.3 (2010), pp. 2008–2011. ISSN: 00036951. DOI: 10.1063/1.3467052.

[3] W. Beyer et al. "Voids in hydrogenated amorphous silicon materials." In: *Journal of Non-Crystalline Solids* 358.17 (2012), pp. 2023–2026. ISSN: 00223093. DOI: 10.1016/j.jnoncrysol.2011.09.030. URL: http://dx.doi.org/10.1016/j.jnoncrysol.2011.09.030.

[4] Christian Bohling and Wolfgang Sigmund. "Self-Limitation of Native Oxides Explained." In: *Silicon* 8.3 (2016), pp. 339–343. ISSN: 18769918. DOI: 10.1007/s12633-015-9366-8. URL: http://dx.doi.org/10.1007/s12633-015-9366-8.

[5] M. H. Brodsky, Manuel Cardona, and J. J. Cuomo. "Infrared and Raman spectra of the silicon-hydrogen bonds in amorphous silicon prepared by glow discharge and sputtering." In: *Physical Review B* 16.8 (1977), pp. 3556–3571. ISSN: 01631829. DOI: 10.1103/PhysRevB.16.3556.

[6] Steven J. Byrnes. *Multilayer optical calculations*. Tech. rep. 2016, pp. 1–20. URL: http://arxiv.org/abs/1603.02720.

[7] M. Cardona. "Vibrational Spectra of Hydrogen in Silicon and Germanium." In: *Physica Status Solidi (B)* 118.2 (1983), pp. 463–481. ISSN: 15213951. DOI: 10.1002/pssb.2221180202.

[8] G. Cataldo et al. "Second-Generation Design of Micro-Spec: A Medium-Resolution, Submillimeter-Wavelength Spectrometer-on-a-Chip." In: *Journal of Low Temperature Physics* 193.5-6 (2018), pp. 923–930. ISSN: 15737357. DOI: 10.1007/s10909-018-1902-7. URL: https://doi.org/10.1007/s10909-018-1902-7.

[9] F. Chaibi et al. "The effects of argon and helium dilution in the growth of nc-Si:H thin films by plasma-enhanced chemical vapor deposition." In: *Journal of Materials Science* 53.5 (2018), pp. 3672–3681. ISSN: 15734803. DOI: 10.1007/s10853-017-1791-1.

[10] A. Endo et al. "On-chip filter bank spectroscopy at 600-700 GHz using NbTiN superconducting resonators." In: *Applied Physics Letters* 103.3 (2013). ISSN: 00036951. DOI: 10.1063/1.4813816.

[11] Akira Endo et al. "Wideband on-chip terahertz spectrometer based on a superconducting filterbank." In: (2019).

[12] Michael Y. Frankel et al. "Terahertz Attenuation and Dispersion Characteristics of Coplanar Transmission Lines." In: *IEEE Transactions on Microwave Theory and Techniques* 39.6 (1991), pp. 910–916. ISSN: 15579670. DOI: 10.1109/22.81658.

[13] Jabbar Ganji, Abdolnabi Kosarian, and Hooman Kaabi. "Mathematical Evaluation of a-Si:H Film Formation in rf-PECVD Systems." In: *Silicon* (2019). ISSN: 1876-990X. DOI: 10.1007/s12633-019-00167-9.

[14] Jiansong Gao. "The Physics of Superconducting Microwave Resonators." PhD thesis. California Institute of Technology, 2008. DOI: 10.1088/0031-9120/1/1/306.

[15] Jiansong Gao et al. "Experimental evidence for a surface distribution of two-level systems in superconducting lithographed microwave resonators." In: *Applied Physics Letters* 92.15 (2008), p. 152505. ISSN: 0003-6951. DOI: 10.1063/1.2906373.

[16] Daxing Han et al. "Raman study of thin films of amorphous-to-microcrystalline silicon prepared by hot-wire chemical vapor deposition." In: *Journal of Applied Physics* 94.5 (2003), pp. 2930–2936. ISSN: 0021-8979. DOI: 10.1063/1.1598298.

[17] R.W. Jackson. "Coplanar Waveguide Vs. Microstrip for Millimeter Wave Integrated Circuits." In: *IEEE MTT-S Digest* (1986), pp. 699–702. DOI: 10.1109/mwsym.1986.1132285.

[18] Wolfgang Jacob, Achim vom Keudell, and Thomas Schwarz-Selinger. "Infrared analysis of thin films: amorphous, hydrogenated carbon on silicon." In: *Brazilian Journal of Physics* 31.1 (2001), pp. 109–109.

[19] Tsutomu Kaneko et al. "FTIR analysis of a-SiC:H films grown by plasma enhanced CVD." In: *Journal of Crystal Growth* 275.1-2 (2005), pp. 1097–1101. ISSN: 00220248. DOI: 10.1016/j.jcrysgro.2004.11.128.

[20] Charalambos C. Katsidis and Dimitrios I. Siapkas. "General transfer-matrix method for optical multilayer systems with coherent, partially coherent, and incoherent interference." In: *Applied Optics* 41.19 (2002), p. 3978. ISSN: 0003-6935. DOI: 10.1364/ao.41.003978.

[21] K. Kouwenhoven. "Dielectric Loss Measurement at Sub-K Temperatures and Terahertz Frequencies." PhD thesis. TU Delft, 2019.

[22] A. A. Langford, M. L. Fleet, and B P Nelson. "Infrared absorption strength and hydrogen contetn of hydrogenated amorphous silicon." In: *Physical Review B* 45.23 (1992). DOI: 10.1016/B978-0-12-809597-3.00260-1.

[23] Young Joo Lee et al. "Structural characterization of wavelength-dependent Raman scattering and laser-induced crystallization of silicon thin films." In: *Thin Solid Films* 542 (2013), pp. 388–392. ISSN: 00406090. DOI: 10.1016/j.tsf.2013.06.055. URL: http://dx.doi.org/10.1016/j.tsf.2013.06.055.

[24] Xiao Liu and R. Pohl. "Low-energy excitations in amorphous films of silicon and germanium." In: *Physical Review B - Condensed Matter and Materials Physics* 58.14 (1998), pp. 9067–9081. ISSN: 1550235X. DOI: 10.1103/PhysRevB.58.9067.

[25] Xiao Liu et al. "Amorphous solid without low energy excitations." In: *Physical Review Letters* 78.23 (1997), pp. 4418–4421. ISSN: 10797114. DOI: 10.1103/PhysRevLett.78.4418.

[26] Xiao Liu et al. "Hydrogen-free amorphous silicon with no tunneling states." In: *Physical Review Letters* 113.2 (2014), pp. 1–5. ISSN: 10797114. DOI: 10.1103/PhysRevLett.113.025503.

[27] N. Maley. "Critical investigation of the infrared-transmission-data analysis of hydrogenated amorphous silicon alloys." In: *Physical Review B* 46.4 (1992), pp. 2078–2085.

[28] Benjamin A Mazin. "Microwave Kinetic Inductance Detectors." PhD thesis. California Institute of Technology, 2004.

[29] Benjamin A. Mazin et al. "Thin film dielectric microstrip kinetic inductance detectors." In: *Applied Physics Letters* 96.10 (2010), pp. 3–5. ISSN: 00036951. DOI: 10.1063/1.3314281.

[30] Puspashree Mishra and K. P. Jain. "First- and second-order Raman scattering in nanocrystalline silicon." In: *Physical Review B - Condensed Matter and Materials Physics* 64.7 (2001), pp. 733041–733044. ISSN: 01631829. DOI: 10.1103/PhysRevB.64.073304.

[31] Valery P. Mitrofanov et al. "Technology for the next gravitational wave detectors." In: *Science China: Physics, Mechanics and Astronomy* 58.12 (2015), pp. 1–26. ISSN: 16747348. DOI: 10.1007/s11433-015-5738-8.

[32] G. Morell et al. "Characterization of the silicon network disorder in hydrogenated amorphous silicon carbide alloys with low carbon concentrations." In: *Journal of Non-Crystalline Solids* 194.1-2 (1996), pp. 78–84. ISSN: 00223093. DOI: 10.1016/0022-3093(95)00459-9.

[33] K. Mui and F. W. Smith. "Optical dielectric function of hydrogenated amorphous silicon: Tetrahedron model and experimental results." In: *Physical Review B* 38.15 (1988), pp. 10623–10632. ISSN: 01631829. DOI: 10.1103/PhysRevB.38.10623.

[34] Clemens Müller, Jared H Cole, and Jürgen Lisenfeld. "Towards understanding two-level-systems in amorphous solids: insights from quantum circuits." In: *Reports on Progress in Physics* 82.12 (Oct. 2019), p. 124501. DOI: 10.1088/1361-6633/ab3a7e. URL: https://doi.org/10.1088%2F1361-6633%2Fab3a7e.

[35] G.A. Niklasson, C.G. Granqvist, and O. Hunderi. "Effective medium models for the optical properties of inhomogeneous materials." In: *Applied Optics* 20.1 (1981), pp. 26–30. ISSN: 0964-9271. DOI: 10.12968/pnur.2008.19.3.28741.

[36] Aaron D. O'Connell et al. "Microwave dielectric loss at single photon energies and millikelvin temperatures." In: *Applied Physics Letters* 92.11 (2008), pp. 11–13. ISSN: 00036951. DOI: 10.1063/1.2898887.

[37] J. Daey Ouwens and R. Schropp. "Hydrogen microstructure in hydrogenated amorphous silicon." In: *Physical Review B - Condensed Matter and Materials Physics* 54.24 (1996), pp. 17759–17762. ISSN: 1550235X. DOI: 10.1103/PhysRevB.54.17759.

[38] W. A. Phillips. "Tunneling states in amorphous solids." In: *Journal of Low Temperature Physics* 7.3-4 (1972), pp. 351–360. ISSN: 00222291. DOI: 10.1007/BF00660072.

[39] Robert O. Pohl, Xiao Liu, and Eun Joo Thompson. "Low temperature thermal conductivity and acoustic attenuation in amorphous solids." In: *Reviews of Modern Physics* 74.4 (2002), pp. 991–1013. ISSN: 00346861. DOI: 10.1103/RevModPhys.74.991.

[40] D. R. Queen et al. "Excess specific heat in evaporated amorphous silicon." In: *Physical Review Letters* 110.13 (2013), pp. 1–5. ISSN: 00319007. DOI: 10.1103/PhysRevLett.110.135901.

[41] D. R. Queen et al. "Two-level systems in evaporated amorphous silicon." In: *Journal of Non-Crystalline Solids* 426 (2015), pp. 19–24. ISSN: 00223093. DOI: 10.1016/j.jnoncrysol.2015.06.020. URL: http://dx.doi.org/10.1016/j.jnoncrysol.2015.06.020.

[42] C. Ricciardi et al. "Microstructure analysis of a-SiC:H thin films grown by high-growth-rate PECVD." In: *Journal of Non-Crystalline Solids* 352.9-20 SPEC. ISS. (2006), pp. 1380–1383. ISSN: 00223093. DOI: 10.1016/j.jnoncrysol.2005.11.137.

[43] P. M. Sarro et al. "Low-stress PECVD SiC thin films for IC-compatible microstructures." In: *Sensors and Actuators, A: Physical* 67.1-3 (1998), pp. 175–180. ISSN: 09244247. DOI: 10.1016/S0924-4247(97)01730-5.

[44] E. Shirokoff et al. "Design and performance of SuperSpec: An on-chip, KID-based, mm-wavelength spectrometer." In: *Journal of Low Temperature Physics* 176.5-6 (2014), pp. 657–662. DOI: 10.1007/s10909-014-1122-8.

[45] A. H. M. Smets, W. M. M. Kessels, and M. C. M. van de Sanden. "Vacancies and voids in hydrogenated amorphous silicon." In: *Applied Physics Letters* 82.10 (2003), pp. 1547–1549. ISSN: 0003-6951. DOI: 10.1063/1.1559657.

[46] C. Smit et al. "Determining the material structure of microcrystalline silicon from Raman spectra." In: *Journal of Applied Physics* 94.5 (2003), pp. 3582–3588. ISSN: 00218979. DOI: 10.1063/1.1596364.

[47] Olaf Stenzel. *The Physics of Thin Film Optical Spectra: An Introduction*. 2015, p. 43. ISBN: 9783540231479.

[48] R.A. Street. *Hydrogenated Amorphous Silicon*. Vol. 2001, p. 43. ISBN: 9780521371568.

[49] R Swanepoel. "Determination of surface roughness and optical constants of inhomogeneous amorphous silicon films." In: *Journal of Physics E: Scientific Instruments* 17.10 (1984), p. 896. URL: http://stacks.iop.org/0022-3735/17/i=10/a=023.

[50] M. B. Tzolov, N. V. Tzenov, and D. I. Dimova-Malinovska. "Analysis of the infrared transmission data of amorphous silicon and amorphous silicon alloy films." In: *Journal of Physics D: Applied Physics* 26.1 (1993), pp. 111–118. ISSN: 13616463. DOI: 10.1088/0022-3727/26/1/018.

[51] R. L.C. Vink, G. T. Barkema, and W. F. van Der Weg. "Raman spectra and structure of amorphous Si." In: *Physical Review B - Condensed Matter and Materials Physics* 63.11 (2001). ISSN: 1550235X. DOI: 10.1103/PhysRevB.63.115210.

[52] Pieter de Visser. "Quasiparticle dynamicsin aluminium superconducting microwave resonators." PhD thesis. 2014.

[53] V. A. Volodin and D. I. Koshelev. "Quantitative analysis of hydrogen in amorphous silicon using Raman scattering spectroscopy." In: *Journal of Raman Spectroscopy* 44.12 (2013), pp. 1760–1764. ISSN: 03770486. DOI: 10.1002/jrs.4408.

[54] P W. Anderson, B I Halperin, and C M. Varma. "Philosophical Magazine HP." In: *The Philosophical Magazine: A Journal of Theoretical Experimental and Applied Physics* 25.1 (1972), pp. 1–91.

[55] Christopher K. Walker. *Terahertz Astronomy*. 2015. DOI: 10.1201/b19111.

[56] J Wenner et al. "Surface loss simulations of superconducting coplanar waveguide resonators." In: *Applied Physics Letters* 99.11 (2011), p. 113513. ISSN: 0003-6951. DOI: 10.1063/1.3637047.

[57] W. Woods et al. "Determining Interface Dielectric Losses in Superconducting Coplanar-Waveguide Resonators." In: *Physical Review Applied* 12.1 (2019), p. 1. ISSN: 2331-7019. DOI: 10.1103/physrevapplied.12.014012. URL: https://doi.org/10.1103/PhysRevApplied.12.014012.

[58] John Woollam et al. "Overview of Variable Angle Spectroscopic Ellipsometry Part I." In: *Proceedings of SPIE - The International Society for Optical Engineering* June (1999).